PARTITIONING MOLECULAR AND SURFACE ENVIRONMENTS: PRACTICE AND APPROXIMATIONS

A Dissertation

Presented to the Faculty of the Graduate School

of Cornell University

in Partial Fulfillment of the Requirements for the Degree of

Doctor of Philosophy

by

Kathleen Schwarz

May 2014

PARTITIONING MOLECULAR AND SURFACE ENVIRONMENTS: PRACTICE AND APPROXIMATIONS

Kathleen Schwarz, Ph.D.

Cornell University 2014

The physics of complex environments, though poorly understood, plays a critical role in a wide range of systems from the biological to the technological. Despite the importance of these systems, they are poorly understood. The large required simulation size of complex environments currently makes them unsuitable for direct *ab initio* calculations, yet inexpensive methods such as molecular modeling can be too approximate to describe the relevant chemical interactions. One resolution to this problem is to accurately describe specific interactions, and to inexpensively approximate interactions which are less relevant. The objective of this thesis is to determine to what extent one can partition systems into a molecule or surface treated at one level of theory, and a surrounding fluid or other molecular environment treated with another theory. I explore varying levels of theory, using different theories depending on the properties of the system and type of problem, and I address conflicts that arise from these choices when working to calculate properties of real systems.

In the first project of the thesis, I strategically explore very different levels of theory for the solvent and solute to subvert the typical relationship found in computational work between cost and accuracy. In this thesis chapter, I combine a simple continuum description of a fluid with highly accurate quantum Monte Carlo calculations, to find solvation free energies of molecules. I find that this approach successfully preserves the accuracy of quantum Monte Carlo, while creating a framework for future calculations with more complicated fluid models.

In the next two chapters, I investigate the continuum between expensive calculations of realistic systems, and inexpensive idealized systems. I examine the properties of lithium-sulfur battery systems and defects in pentacene thin films, using established polarizable continuum methods and density-functional theory, exploring the extent to which experimental realities alter the relevant observables. I am able to produce idealized voltammograms that capture key aspects of the battery experiments, and I also identify an experimentally observed defect in the pentacene.

In the last chapter, I investigate the creation of a whole crystal from the sum of its parts, as I develop approximations of the dielectric matrix in molecular crystals. I successfully apply this to two crystals, creating dielectric band structures from molecular calculations that very closely resemble those from the entire crystal.

BIOGRAPHICAL SKETCH

The author was born on October 25, 1984, in Tallahassee, Florida. She attended Washington University in St. Louis, graduating with a B.A. in Chemistry, in 2007. In 2007, she began her graduate studies at Cornell University in the Department of Chemistry and Chemical Biology.

This document is dedicated to my family and lab family, for their help and support during my time at Cornell.

ACKNOWLEDGEMENTS

I would like to thank Tomás Arias for training me to be a better scientist, and for encouraging me to explore areas of science beyond where I was most comfortable. Thanks also to the Arias research group that warmly welcomed me when I joined their group- to JeeHye Lee, Kendra Letchworth-Weaver, and Ravishankar Sundararaman for their friendship, help, solidarity, support, and discussion. Thank you to my other thesis committee members- to John Marohn and Richard Hennig for their collaboration and helpful discussions, and to Roald Hoffmann for his sharing his insights and chemical intuition, especially during Hoffmann group meetings. I would also like to thank my extended family members who supported me while finishing up- especially Elsa Labonski and Marlow Schwarz.

TABLE OF CONTENTS

LIST OF TABLES

LIST OF FIGURES

CHAPTER 1

INTRODUCTION

1.1 Motivation

Solvation is an essential process, necessary for diverse activities from fuel cell and battery operation, to life itself. While experimental efforts have progressed towards an understanding of solvated systems, even the interactions of surfaces and water, the "universal solvent", remain incompletely understood. For individual molecules and surfaces, *ab initio* computational studies hold the promise of relatively rapid, accurate, and inexpensive results, but the introduction of solvation can lead to complex and expensive calculations. *Ab initio* calculations coupled with a solvation model have the potential to provide a tractable way forward, bringing the advantages of *ab initio* calculations, with less cost and complexity.

The objective of this thesis is to explore to what extent one can partition systems into a molecule or surface treated at one level of theory, and a surrounding fluid or other molecular environment treated with another level of theory. I explore various levels of theory for both the solvent and the solute, altering my choice of theory depending on both the type of problem, and the properties of the system, addressing the conflicts and complexity that arise from these choices when calculating properties of real systems. For the solvent, I explore varying levels of theory- from the empirical polarizable continuum model, to the rigorous Joint Density-Functional theory, and even to a new theory specially developed for the approximation of dielectric properties. For the solute, I explore a wide range of physical properties, including chemical equilibria, optical spectra, and dielectric properties.

Ab initio techniques have been successfully applied to simple crystals and gas phase molecules, but complex liquid and solid environments are frequently beyond the reach of these methods. In Chapter 1, I review the main techniques employed in this thesis, most notably *ab initio* electronic structure methods, including quantum Monte Carlo and density-functional theory. I then review techniques for describing solvation, focusing on Joint Density-Functional Theory, with a concluding section on the noninteracting dielectric response function.

Chapter 2 discusses the implementation of the framework of Joint Density-Functional theory into quantum Monte Carlo. In this chapter, I combine highly accurate quantum Monte Carlo calculations with an inexpensive fluid model to find solvation free energies of molecules. The work in this chapter was originally published in Physical Review B, as "Framework for solvation in quantum Monte Carlo", by Kathleen Schwarz, Ravishankar Sundararaman, Kendra Letchworth-Weaver, and T.A. Arias. Employing a classical density-functional description of liquid environments, I introduce a rigorous method for the diffusion quantum Monte Carlo calculation of free energies and thermodynamic averages of solvated systems that requires *neither* thermodynamic sampling *nor* explicit solvent electrons. I find that this method yields promising results and small convergence errors for a set of test molecules. It is implemented readily and is applicable to a range of challenges in condensed matter, including the study of transition states of molecular and surface reactions in liquid environments.

Chapter 3 is an investigation of lithium sulfur battery systems, as a preliminary step towards a theoretical understanding of sulfur anion equilibrium and disproportionation. In this chapter, the impact of solvation effects on sulfur anion equilibrium and oxidation/reduction voltage are studied. The dielectric constant and ionic character of the solvent are found to strongly influence the predicted species present at equilibrium. The

dielectric constant is a particularly important influence in the $S_3^{1-} \leftrightharpoons S_6^{2-}$ equilibrium. Idealized voltammograms are also created in this chapter, and effects of the solvent, especially ionic effects, are found to significantly alter the predicted sulfur oxidation and reduction voltages. The predicted behavior of the sulfur oxidation/reduction agrees well with observations from recently published experimental work.

Chapter 4 utilizes the polarizable continuum model in time dependent density-functional calculations as an approximation for the molecular crystalline environment of a pentacene thin film. The work in this chapter was originally published in Advanced Materials as "Spectroscopic Characterization of Charged Defects in Polycrystalline Pentacene by Time- and Wavelength-Resolved Electric Force Microscopy" by Justin Luria, Kathleen Schwarz, Michael Jaquith, Richard Hennig, and John Marohn. In this work, I perform calculations of defect molecules in a pentacene thin film to examine their energy levels and spectroscopic properties, to attempt to identify the experimentally observed defect. The calculations helped to identify a defect percursor, pentacen-6(13H)-one, which can account for the experimental observations.

Chapter 5 develops a method for approximating dielectric properties of molecular environments, without the use of a polarizable continuum. The dielectric response function for a single molecule in the system is calculated, and this response function is rotated and translated to approximate the response functions of all of the other molecules in the system. This approach was successfully applied to calculate both the hexagonal ice and the solid benzene *dielectric* band structures.

1.2 Methods

In this section, I discuss the key methods used in my thesis. I begin with a broad discussion of electronic structure, including both quantum Monte Carlo methods and density-functional theory. I then discuss solvation, and the connection between density-functional theory and the solvation method known as Joint Density-Functional Theory. I end the section with a derivation of the noninteracting microscopic polarizablity response function, a key starting point for the study of dielectric properties in Chapter 5.

1.2.1 *Ab Initio* Electronic Structure

The fundamental relationship in *ab initio* electronic structure is the time-independent Schrodinger equation, written in Dirac notation as

$$\hat{H}|\psi\rangle = E|\psi\rangle, \tag{1.1}$$

where E is the energy of the system, H is the Hamiltonian operator, and ψ is the many-body wavefunction that represents a solution to this equation. The Hamiltonian operator for non-relativistic atoms and electrons interacting through electromagnetic forces can be written as:

$$\hat{H} = -\frac{1}{2m_i}\sum_{i=1}^{N}{\nabla_i}^2 + \sum_{i=1,j>i}^{N}\frac{c_i c_j}{r_{ij}} + \sum_{i=1}^{N}V(r_i), \tag{1.2}$$

where we work in standard atomic units where $k_C e^2 = 1$ hartree-bohr, $\hbar^2/m_e = 1$ hartree-bohr^2, we measure all masses are measured in units of the electron mass m_e, and 1 hatree$\approx$27.21 eV, 1 bohr$\approx$0.5292 Å. The first term is the sum of the kinetic energies of each particle i, and N is the total number of particles. The second term is the sum of

the Coulombic interactions between all pairs of particles i and j, and the c represents the charge of the particle. The third term, V(r), is a potential representing any external field.

The mass difference between the electron and the nucleus allows one to approximately separate the nuclear and electronic components of this equation via the Born-Oppenheimer approximation. The equation can now be written as:

$$\hat{H} = -\frac{1}{2}\sum_{i=1}^{n} {\nabla_i}^2 + \sum_{i=1,j>i}^{n} \frac{1}{r_{ij}} - \sum_{I=1}^{N}\sum_{i=1}^{n} \frac{Z_I}{r_{Ii}} + E_{nuc} + \sum_{i=1}^{n} V(r), \tag{1.3}$$

where the first term is the electronic kinetic energy, the second term is the electron-electron potential energy, the third term is the nucleus-electron potential energy, and the fourth term is the energy of the nuclear potential and kinetic energies.

The Hamiltonian derived above in Eq. 1.3 has not been solved for many electrons with multiple nuclei — the exact wavefunction required to solve a system of many interacting electrons and nuclei has not been found. Instead, numerical methods of approximating the wavefunction, and methods to approximate the Hamiltonian to create more tractable problems have been developed. First, I detail a numerical approach to approximating the wavefunction through quantum Monte Carlo methods. I then describe the concepts behind and the approximations frequently employed in density-functional theory.

1.2.2 Quantum Monte Carlo

Quantum Monte Carlo refers to multiple theories that use Monte Carlo methods to numerically evaluate integrals and approximate wavefunctions used in electronic structure theory. The two quantum Monte Carlo methods used in this thesis are variational Monte Carlo (VMC) and diffusion Monte Carlo (DMC).

Using the Hamiltonian of Eq. 1.3, the energy of an approximate or exact wavefunction can be written as

$$E = \frac{\langle \psi | H | \psi \rangle}{\langle \psi | \psi \rangle}. \tag{1.4}$$

Given a wavefunction and a basis, this energy can be numerically evaluated using weighted Monte Carlo sampling. This is the fundamental idea behind variational Monte Carlo. Specifically, a quantity known as the 'local energy',

$$E_L(R) = \frac{H\psi_T(R)}{\psi_T(R)}, \tag{1.5}$$

where $\psi_T(R)$ is the trial wave function, is sampled at electron configurations weighted by the probability density, and the average value of this local energy is the estimate of the energy. Trial wave functions are typically composed of two parts: (1) a wavefunction acquired from another method such as Hartree Fock or configuration interaction, and (2) Jastrow factors with optimizable parameters typically used to capture the dynamic correlation that methods such as Hartree Fock miss. Thus, when used with a Slater determinant without a Jastrow factor, variational Monte Carlo is equivalent to Hartree Fock. The accuracy of variational Monte Carlo results depend on the quality of the trial wave function, which can be improved iteratively through optimization of the parameters in the Jastrow factors. See [20] for further discussion of the variational Monte Carlo method.

Similarly to variational Monte Carlo, diffusion Monte Carlo also requires a trial wavefunction, but in contrast, the trial wavefunction is only the starting point, essentially an initial guess. This 'guess' is then refined using a stochastic projector method to solve the imaginary-time Scrödinger equation. Diffusion Monte Carlo thereby projects out all states but the ground-state from the trial wave function, and the ultimate accuracy of Diffusion Monte Carlo thus does not depend as strongly on the accuracy of the trial wave function as in the case of variational Monte Carlo.

In Diffusion Monte Carlo, the trial wave function is necessary to constrain the projection because, otherwise, the trial wave function would converge to the the bosonic solution. To impose fermionic antisymmetry, one typically imposes the boundary condition that the nodes of the many-body wave function are the same as those of the trial wave function, which is typically acquired from variational Monte Carlo. The resulting error, known as the fixed-node error, can be reduced by improving the trial wave function. The fixed-node error represents one of the major sources of error for diffusion Monte Carlo — if the fixed-node error were absent, the results from diffusion Monte Carlo would be essentially exact. Unlike other potential sources of error, such as the pseudopotential and time-step errors [20], the fixed-node error is not easily corrected or quantified. Nonetheless, comparisons with experiment when available indicate that the errors in diffusion Monte Carlo calculations are typically smaller than the errors associated with most other quantum chemical methods, and chemical accuracy is frequently achieved for small systems.

Hohenberg-Kohn Theorems

Just as quantum Monte Carlo is exact in principle, density-functional theory also contains a formally exact framework. The Hohenberg-Kohn theorems form the basis for density-functional theory. The first theorem is related to the variational principle. If two electronic systems exist in two potentials, $V_1(r)$ and $V_2(r)$, and the two electronic systems share the same ground-state electron density, then the two potentials can only differ by a constant. This can be easily shown. Writing the Hamiltonian as

$$H_1 = H + V_1(r) \tag{1.6}$$

$$H_1 = H + V_2(r) \tag{1.7}$$

and the density as $n(r)$, where we represent the density in the basis of ψ as:

$$n(r) = |\psi(r)\rangle\langle\psi(r)|. \tag{1.8}$$

We can write the energies of the two systems as:

$$H_1 n(r) = E_1 n(r) \tag{1.9}$$

and

$$H_2 n(r) = E_2 n(r) \tag{1.10}$$

Subtracting the two equations, we see that

$$(H_1 - H_2)n(r) = (E_1 - E_2)n(r), \tag{1.11}$$

which is equivalent to:

$$V_1(r) - V_2(r) = E_1 - E_2, \tag{1.12}$$

demonstrating that the potentials can only differ by a constant. This theorem means that the ground-state density, a position dependent function, determines all of the properties of the system. For systems with more than one electron, the density is a much simpler quantity than the many-body wave function, which is a function of each of the electron's coordinates and electron spin states.

The second theorem states that a density-functional exists for any number of electrons, that, when minimized, results in the ground-state energy and density of the system: the value of the functional at the minimum corresponds to the ground-state energy of the system and the minimizing density gives the electron density in the ground state. This can be written as the energy variational principle,

$$E_o \leq E_v[\rho], \tag{1.13}$$

where E_o is the ground-state energy of the system, and $E_v[\rho]$ is the energy associated with any trial density ρ.

The exactness of the Hohenberg-Kohn-Sham theorems forms the framework for density-functional theory, but it does not provide a functional form for $E_v[\rho]$. One way to proceed is with the Kohn-Sham method, an approach which allows for orbital-based calculations.

The Kohn-Sham Theorem

The groundbreaking idea behind the Kohn-Sham method is that a reference system of noninteracting electrons in an external potential could have exactly the same density as the ground-state density for a system of interacting electrons [60]. Using this concept, single-electron equations can be written,

$$[-\frac{\nabla^2}{2} + v_{\text{eff}}]\psi_i = \epsilon\psi_i, \tag{1.14}$$

with the density defined as

$$\rho(r) = \sum_i^N \sum_s |\psi_i(r, s)|^2, \tag{1.15}$$

where N is the number of electrons and s is the spin. Finally, the effective potential v_{eff} is defined self-consistently as

$$v_{\text{eff}} = v(r) + \frac{\delta E_{xc}[\rho]}{\delta\rho(r)} + \int dr' \frac{\rho(r')}{|r - r'|}. \tag{1.16}$$

Here, the exchange-correlation energy functional E_{xc} contains exactly all energy contributions beyond the mean-field Hartree energy, including corrections to the electrostatic and kinetic energies of the electron gas due to correlations from both statistical correlations from Fermi statistics ("exchange") and dynamical correlations from Coulomb repulsion ("correlation").

The exact formulation of the exchange-correlation density-functional is unknown, although very good approximations continue to be developed. Arguably the two most

widely known and applied exchange-correlation functionals are the local-density approximation (LDA) and the generalized gradient approximation (GGA). The local-density approximation defines the exchange correlation energy as

$$E_{xc}^{LDA}[\rho] = \int dr\, \rho(r)\epsilon_{xc}(\rho), \tag{1.17}$$

where $\epsilon_{xc}(\rho)$ is the exchange correlation energy of a single particle in a uniform electron gas with density ρ. The generalized gradient approximation expands on the local-density approximation to include the dependence of the single particle's energy on the gradient of the density. These approximations work well for the energies of molecules and atoms, but when these approximations fail, the errors are not as predictable as the statistical errors seen in quantum Monte Carlo calculations. For instance, a recent study comparing density functional theory methods with diffusion Monte Carlo found that for a set of benchmark solids, the calculated equilibrium volumes had errors from the local density approximation of up to nearly 20%, whereas the quantum Monte Carlo results had less than 10% errors compared to experimental values [74].

Solvation methods

Methods such as quantum Monte Carlo and density-functional theory provide ways to approximate the behavior of electrons near nuclei, but they are not inexpensive, scaling approximately as n^3, where n is the number of electrons in the system. Other approximations are frequently needed when the system in question contains many (moving) nuclei whose locations and arrangements must be samples statistically, resulting in the needs for thousands of already quite challening calculations. As a result, for these calculations including solvation, the solute is frequently described at one level of theory, such as the electronic structure methods described above, and the solvent is treated at a lower level of theory.

At a molecular level, solvation is a dynamic equilibrium between a solute and different configurations of solvent molecules, yet an understanding of this process has long been elusive. With the advent of electrochemical cells, and the beginnings of the field of electrochemistry, ideas about the solvation (at least of ions) became easily testable. By 1903, it was widely acknowledged that ions frequently dissociate in solvent, despite the strong Coulombic forces, and Svante Arrhenius won the Nobel prize for his work towards this conclusion [4]. However, it was not until much later, around the 1930's and 1940's, that the molecular interactions involved in solvation began to be probed [58]. At this point, a dichotomy had developed between the earlier conception of solvent as a dielectric continuum, and the newly investigated, and sometimes well-characterized, solvent shells around ions and molecules in solution. These differing conceptions of solvation continue in computational studies, with some approaches focused on the molecular nature of the solvent, and others emphasing a continuum interpretation of the solvent.

Solvation by explicit inclusion of solvent molecules has historically been used by the chemistry community to study reactions and reaction mechanisms, yet this approach ignores the ensemble nature of the problem. Molecular dynamics addresses this issue, but the necessary thermodynamic phase space sampling can be expensive, with multiple thousands of *ab initio* calculations required.

Solvation of molecular systems is most commonly approximated as a continuum in the popular polarizable continuum model, now sometimes referred to as DPCM, the dielectric polarizable continuum model [85]. Continuum solvation models include at a minimum a dielectric continuum which interacts with the solute which is regarded to sit at the center of a cavity in the dielectric medium. Definitions for the cavity range from a simple single sphere, to a cavity based on the self-consistent electron density of the solute [85]. A cavity based on pre-determined parameters is utilized for work

in Chapters 3 and 4, and an isodensity cavity is utilized for work in Chapter 2. It is important to note that the continuum model discussed and applied in Chapter 2 utilizes a framework for solvation, Joint Density-Functional Theory, which is distinct from the PCM approaches in its derivation, scope, and rigorous theoretical foundation.

The fundamental principle of Joint Density-Functional theory is that the thermodynamics of a solvent-solute system can be described in principle exactly (in the same sense of the Hohenberg-Kohn theorems) by a joint functional of the density of the solute electrons and the density of the atomic species which make up the molecules [61]. Specifially, a free-energy variational principle can be written as

$$A[n, \{N_\alpha\}] = A_{\mathrm{HK}}[n] + \Phi_{\mathrm{lq}}[\{N_\alpha\}] + \Delta A[n, \{N_\alpha\}], \tag{1.18}$$

where $A_{\mathrm{HK}}[n]$ is the electronic Hohenberg-Kohn free-energy functional for the explicit system in isolation, Φ_{lq} is the free-energy functional for the liquid when in isolation, and ΔA is the coupling between the explicit system and the solvent. In parallel to the ground-state Hohenberg-Kohn theorems, the minimum value of this functional yields the thermodynamic free energy of the solute-solvent system and the minimizing densities give the quantum and *thermodynamically* averaged electron and atomic site densities, respectively.

Just as in Hohenberg-Kohn-Sham theory, the exact form of the various functionals in (2.1) is unknown, particularly the new, coupling functional ΔA. This is an area of active research, and different coupling terms have been explored. The approximate free-energy functional for the liquid has also been investigated, from continuum fluid approaches [62] to classical density functional theory approaches [83, 80, 46].

Continuum solvation has long been used in quantum chemistry calculations [85], but it is infrequently utilized in plane-wave calculations. With the advent of smoothly varying isodensity polarizable continuum models, implicit solvation plane wave calcu-

lations became feasible [17, 62], but implicit solvation is still not widely implemented into commercial plane-wave software packages. Chapter 2 discusses the implementation of continuum solvation for quantum Monte Carlo calculations from plane wave density-functional theory calculations.

1.2.3 The Noninteracting Microscopic Polarizability

Continuum solvation models are extremely useful for describing solutions, and sometimes even for approximating crystalline environments, but they are not always sufficient for describing complex environments, especially when optical or dielectric properties are observed. In Chapter 5, I develop a method for capturing the dielectric properties of a crystalline environment starting from calculations on a single molecule. However, Chapter 5 uses properties of dielectric materials which may not be familiar to the reader, so here I review the starting point from standard dielectric response theory — the non-interacting response function $\chi_{ni}(r, r')$.

Following Reference [30], the non-interacting response function is defined as relating a change in total potential to the change in the electron density, written as

$$\delta\rho(r) = \int dr' \chi_{ni}(r, r')\delta V_{tot}(r'), \tag{1.19}$$

where the total potential is a sum of the external potential and the screening potential. In the non-interacting context, the density is defined as

$$\rho(r) = \sum_i f_i |\psi_i(r)|^2, \tag{1.20}$$

where $\psi_i(r)$ are single-electron orbitals with occupancies ("fillings") $0 \leq f_i \leq 1$. We first rewrite the density perturbation as

$$\delta\rho(r) = \delta(\sum_i f_i |\psi_i(r)|^2), \tag{1.21}$$

and then expand it as

$$\delta\rho(r) = \sum_i f_i \psi_i^*(r)\delta\psi_i(r) + c.c., \tag{1.22}$$

where "c.c." indicated the complex conjugate of the preceding term. We then rewrite $\delta\psi_i(r)$ using first-order perturbation theory

$$\delta\psi_i(r) = \sum_j (1 - f_j)\frac{\int dr'\psi_j^*(r')\delta V_{tot}(r')\psi_i(r')}{\epsilon_i - \epsilon_j}\psi_j(r), \tag{1.23}$$

where the factor $(1 - f_j)$ reflects both the fact that $j \neq i$ (Recall that $f_i = 1$ for all states contributing to the density.) and the fact that unitary transformation (e.g., mixing) among the filled states leaves the total density unchanged. Inserting this into the density equation yields

$$\delta\rho(r) = \sum_i f_i\psi_i^*(r) \sum_j (1 - f_j)\frac{\int dr'\psi_j^*(r')\delta V_{tot}(r')\psi_i(r')}{\epsilon_i - \epsilon_j}\psi_j(r) + c.c. \tag{1.24}$$

Finally, comparing to the definition for the response function (1.19), we can read off the response function as

$$\chi_{ni}(r, r') = \sum_{i,j} f_i(1 - f_j)\frac{\psi_i^*(r)\psi_j^*(r')\psi_i(r')\psi_j(r)}{\epsilon_i - \epsilon_j} + c.c.. \tag{1.25}$$

Chapter 5 discusses how to use this as a starting point to obtain the dielectric response of molecular crystals from calculations of just single molecules.

CHAPTER 2

FRAMEWORK FOR SOLVATION IN QUANTUM MONTE CARLO

2.1 Introduction

While the exact methods discussed in the last chapter would ideally be used for all calculations of molecules and materials, a large computational expense is associated with highly accurate methods. This chapter[1] develops a method for treating the most important part of a system with the highly accurate (and expensive) quantum Monte Carlo method, and the less important part of the system with a solvation model. The results demonstrate the utility of this method for the test case of molecules solvated in water.

The physics of solvation, though poorly understood, plays a critical role in a wide range of systems from the biological to the technological. For example, the pathways in protein folding [42, 67, 18] and transition states of ionic reactions [38, 65] are known to be highly solvent dependent. Development of a fundamental understanding of the kinetics which underlie such processes requires an accurate description of the quantum mechanical processes involved in bond breaking and formation in solution.

Unlike less rigorous electronic structure methods, quantum Monte Carlo methods [20] do provide the required accuracy for transition states, reactants, and products needed to give reliable information on reaction pathways. However, a full quantum Monte Carlo treatment, in principle, requires solving Schrödinger's equation for all of the involved solvent molecules, a difficulty radically compounded by the need to sample the phase-space of all thermodynamically relevant configurations of the solvent. This

[1] Portions of written content and figures in this chapter reprinted from the arxiv.org version of the cited paper [71]

Chapter introduces a framework for the treatment of solvation in diffusion Monte Carlo which completely eliminates the need for explicit solvent electrons and such phase-space sampling, while remaining completely *ab initio* and exact in principle — in the same sense in which density-functional theory meets these criteria.

Previous attempts to model the effects of solvation in quantum Monte Carlo fall into two categories: (i) simulation of the environment through molecular dynamics [14, 24], and (ii) introduction of a polarizable continuum [1, 2]. The former approach, in principle, captures molecular-scale effects such as solvation shells and non-local dielectric response. However, molecular dynamics with empirical potentials [14], though benefiting from a simplified description of the solvent, depends on a highly parameterized potential to describe the interactions between molecules. Additionally, such calculations require phase-space sampling, which makes the calculations costly — especially if individual electronic structure calculations for the solute are needed for each fluid configuration. Approaches have been proposed to mitigate this expense within *ab initio* molecular dynamics calculations [24], but this approach also is extremely expensive due to the need to include of all of the solvent electrons and nuclei.

In contrast, the polarizable continuum model (PCM) is a computationally inexpensive tool for approximating solvation energies without phase-space sampling. Unfortunately, this model lacks theoretical justification for the treatment of water as a continuum on molecular length scales, and so does not constitute a truly *ab initio* method. Indeed, the pioneering work on solvation studies within diffusion Monte Carlo electronic structure methods [2] rested on the *ad hoc* introduction of a polarizable medium and required a set of spheres with radii determined empirically. A further, practical disadvantage of the aforementioned PCM approach is that it requires potentially costly statistical evaluation of solvent potentials, and so it has yet to yield meaningful comparisons between

predicted solvation energies and experiment.

Joint density-functional theory [62] circumvents both the inaccuracies inherent in the polarizable continuum model and empirical molecular dynamics and the expense associated with *ab initio* molecular dynamics. This work presents an integrated approach to quantum Monte Carlo calculations within this new, rigorous statistical treatment of the solvent, and introduces a variational theorem which abrogates much of the computational complexity associated with achieving full self-consistency between the solute and the solvent. While our approach in theory requires no adjustable parameters, we employ a simplified, approximate version of the theory in this first demonstration that does require a *single* empirically adjusted parameter.

This *Chapter* begins with a brief review of joint density-functional theory and then describes a quantum Monte Carlo formulation of that theory, compares predictions to solvation data, and shows that self-consistency to within chemical accuracy is achievable with the computational cost of a single quantum Monte Carlo calculation.

2.2 Joint Density-Functional Theory And Quantum Monte Carlo.

Joint density-functional theory [62, 61] states that, in principle, the exact quantum and thermodynamically averaged electronic and nuclear densities and the exact free energy of a solvated system can be obtained by minimization of a universal free-energy functional, without the need to sample explicitly the phase space of all possible configurations of solvent molecules. This minimization is carried out over all realizable average solute electron densities $n(r)$ and average solvent site densities $N_\alpha(r)$. (In the present work, $N_\alpha(r)$ refers to the single-particle densities of the oxygen nuclei and protons comprising the solvent, water.) Note that $n(r)$ here refers only to the electron density of

the solute because the electron density of the solvent need not be considered explicitly. Naturally, the underlying indistinguishability of electrons implies that there is no unique decomposition of the total electron density into solute and solvent contributions. Consequently, the solution to the minimization problem is highly degenerate with many choices for $n(r)$ leading to the same, exact free energy. This complication notwithstanding, the free energy and $N_\alpha(r)$ obtained at the minimum are meaningful and represent the exact free energy and solvent site distribution of the combined system at equilibrium. (See Ref. [61] for a fuller discussion.) Finally, we note that the exact universal functional conveniently decomposes into a sum of three terms,

$$A[n, \{N_\alpha\}] = A_{\mathrm{HK}}[n] + \Phi_{\mathrm{lq}}[\{N_\alpha\}] + \Delta A[n, \{N_\alpha\}], \tag{2.1}$$

where $A_{\mathrm{HK}}[n]$ is the electronic Hohenberg-Kohn free-energy functional for the explicit system in isolation, Φ_{lq} is the free-energy functional for the liquid when in isolation, and ΔA represents the coupling between the explicit system and the solvent. Note that, essentially being the definition of $\Delta A[n, \{N_\alpha\}]$, Eq. (2.1) is exact.

Although Eq. (2.1) is exact in principle, the forms of these three functionals on the right-hand side are unknown and need to be approximated in practice. Generally, such approximations will break the aforementioned degeneracy and select a specific $n(r)$ at the minimum of the approximated functional. In this *Chapter*, we use diffusion Monte Carlo to describe the term $A_{\mathrm{HK}}[n]$, and, for our quantum Monte Carlo implementation of joint density-functional theory, we write the terms related to the environment as

$$A_{\mathrm{env}}[n] \equiv \min_{\{N_\alpha\}} \Big(\Phi_{\mathrm{lq}}[\{N_\alpha\}] + \Delta A[n, \{N_\alpha\}] \Big). \tag{2.2}$$

The variational derivative of Eq. (2.1) with respect to the exact electron density then yields the Euler-Lagrange equation $0 = \delta A/\delta n = \delta(A_{HK} + A_{\mathrm{env}})/\delta n$, which is precisely the equation for the isolated solute system in an external potential $V_{\mathrm{env}} \equiv \delta A_{\mathrm{env}}[n]/\delta n$.

When an external potential is found for which the electron density $n(r)$ apportioned to the solute yields back the same potential through this definition, the self-consistent, exact thermodynamic state of the system will have been found. In principle, this exact solution can be obtained through multiple self-consistent iterations. The main difficulty of a quantum Monte Carlo implementation of A_{HK} in this process is the presence of statistical noise in the resulting electron densities, particularly in regions of low electron density, a problem which also plagues the approach of Ref. [2]. There has been recent progress in reducing this noise [5], but the results are not yet sufficiently clean for use in self-consistent calculations. We therefore now introduce a method to *estimate* the self-consistent solution of our solvation theory *without* evaluation of the electron density within quantum Monte Carlo.

2.3 First-Order Estimator Of Self-Consistency.

A natural starting point for a joint density-functional theory quantum Monte Carlo calculation is a fully self-consistent joint density-functional theory calculation within the local density (LDA) or generalized gradient (GGA) approximation for A_{HK}. Such calculations provide trial wavefunctions for quantum Monte Carlo calculations, and the resulting densities n_{DFT} give estimates for the environment potential $\tilde{V}_{\mathrm{env}} = \delta A_{\mathrm{env}}[n_{\mathrm{DFT}}]/\delta n$. One can then perform a single quantum Monte Carlo calculation of the solute within this estimated potential, yielding both an initial quantum Monte Carlo density n_{QMC} and energy $A_{\mathrm{QMC}}[n_{\mathrm{QMC}}]$. Note that the latter quantity is defined as the quantum Monte Carlo estimate of the functional A_{HK}; i.e., the energy of the solute *without* the energy associated with $\tilde{V}_{\mathrm{env}}$.

The two calculations described in the above paragraph could then be combined to

give a zeroth-order estimate of the free energy of the solvated system as $A_{\rm QMC}[n_{\rm QMC}] + A_{\rm env}[n_{\rm DFT}]$. This, however, loses the benefits of the variational principle because the two terms are not self-consistent in that they are evaluated at different electron densities, and so the resulting estimate is not necessarily an upper bound for the final, converged result. Also, the resulting error is first-order in the errors in the density, rather than second-order, as is usually associated with variational calculations. We can correct for this by evaluating, with errors only in the second-order, $A_{env}[n_{\rm QMC}] = A_{env}[n_{\rm DFT}] + \int d^3r\, \tilde{V}_{env}\,(n_{\rm QMC} - n_{\rm DFT})$ because, by definition, $\tilde{V}_{\rm env} = \delta A_{\rm env}[n_{\rm DFT}]/\delta n$. The final result equals

$$\begin{aligned} A =& A_{\rm QMC}[n_{\rm QMC}] + A_{\rm env}[n_{\rm DFT}] + \\ & \int d^3r \tilde{V}_{\rm env}(r)\,(n_{\rm QMC}(r) - n_{\rm DFT}(r)) + O(\delta n^2), \end{aligned} \tag{2.3}$$

with errors that are second-order in *both* the difference between the exact converged density and the density-functional theory density $n_{\rm DFT}$ *and* the difference between the exact converged density and the first-iteration density $n_{\rm QMC}$. Below, we show that this new approach is operationally nearly as good as full self-consistency, but with the effort of only a single quantum Monte Carlo calculation.

2.4 Implementation.

In this work we demonstrate our solvation technique with a simplified description of the environment, but we stress that it may be employed just as readily with whatever functionals for the liquid become available. We note that the quality of our results now depend on our approximation for A_{env}, which we hope to improve in the future. Specifically, we here employ the isodensity model of Petrosyan *et al.* [62], which is similar to the dielectric model by Fattebert and Gygi [17]. These models take the dielectric con-

stant to be a local function of the electron density that switches smoothly from the value for vacuum at high solute electron densities to the dielectric constant of the bulk liquid for low electron densities. This simplified joint density-functional is similar in spirit to the smoothly transitioning nonlinear polarizable continuum model described in Ref. [1], but here we work in a rigorous framework and also effectively achieve solute-solvent self-consistency. We have implemented our method in the open source code JDFTx [82], interfaced with CASINO [55]. In anticipation of applying our method to large solvated surfaces, we use for our starting point the computationally inexpensive local-density approximation at full solute-solvent self-consistency. Fig. 2.1(a) illustrates the cavity formation for acetone, a small molecule chosen for its well-known experimental solvation energy. Our reported solvation energies include, in addition to the electrostatic components from our simplified electrostatic functional, the cavitation energy shown in Table 2.1, estimated from classical density functional theory following the procedure in Ref. [81] as included in the JDFTx package [82] and employing a functional based on Ref. [32].

The density-functional theory and Hartree-Fock calculations employ pseudopotentials from Burkatzki *et al.* [13] and expand the wave functions in a plane-wave basis with a cutoff energy of 30 H (hartree). The local density approximation is employed for the density functional theory calculations, performed using JDFTx [82], and a simulation box of 40 bohr^3. The quantum Monte Carlo calculations are performed using CASINO [55] and employ a trial wavefunction of a product of a single Slater determinant of density functional orbitals and a Jastrow correlation factor composed of electron-nucleus and electron-electron terms with expansion order eight, and electron-electron-nucleus terms with expansion order three, as described in Ref. [16]. The orbitals and external potential V_{env} are represented by B-splines. The parameters of the Jastrow factor are optimized by variance minimization [88]. The diffusion Monte Carlo time step is

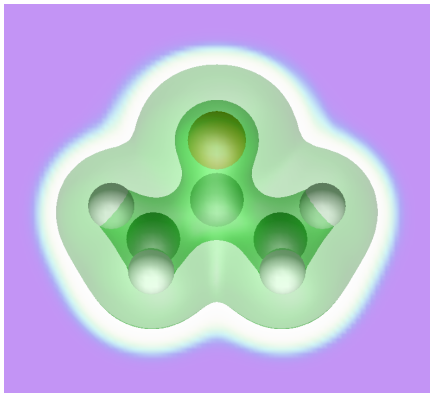

(a)

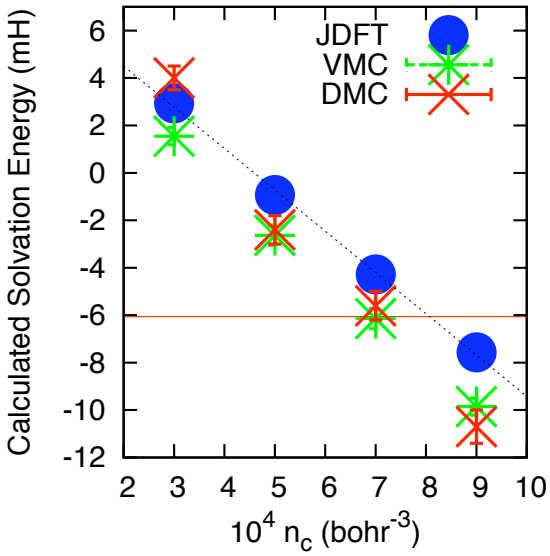

(b)

Figure 2.1: (Color Online) (a) Joint density-functional theory description of acetone in aqueous solution: electron density contours as green (gray) surfaces, solvent as solid purple (dark gray). (b) Solvation energies for acetone: diffusion Monte Carlo (DMC) as red (gray) x's, variational Monte Carlo (VMC) as green (gray) strikethrough x's, Joint Density Functional Theory (JDFT) as blue (gray) circles, Joint Density Functional Theory best fit as a dashed black line, and experiment as a horizontal red (gray) line.

0.01 H^{-1}. (Going from 0.01 to 0.001 H^{-1}, we found the time-step error to be within the statistical uncertainty we report for the solvation energy for acetone in Figure 2.1, with the solvation parameter n_c = 7 x 10^{-4} bohr^{-3}.) Molecular geometries are from the Computational Chemistry Comparison and Benchmark Database: either from experimental data if available, or density-functional optimization using the B3LYP functional and the cc-pVTZ basis set [56].

For the continuum description of water, we use the local dielectric function $\epsilon(n(r)) = 1+(\epsilon_b-1)\,\mathrm{erfc}\left(\ln(\frac{n(r)}{n_c})/(\sqrt{2}\sigma)\right)/2$, where ϵ_b is the bulk dielectric constant of the fluid, n_c specifies the value of the solute electron density at which the dielectric cavity forms, and

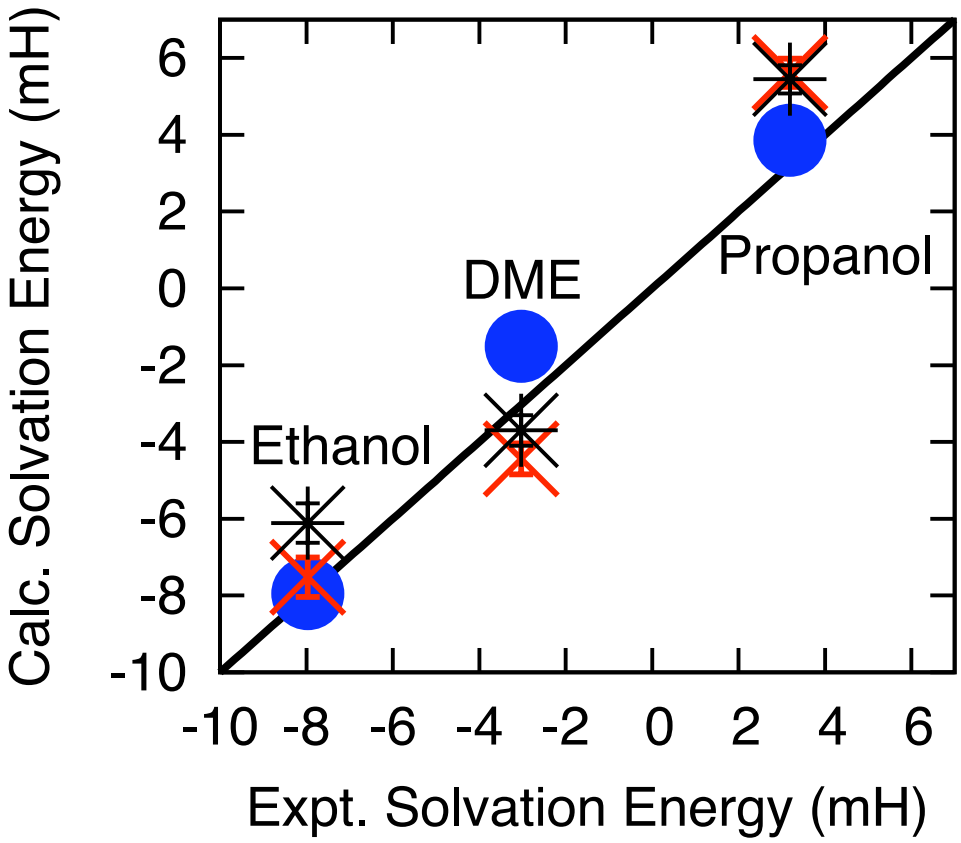

Figure 2.2: (Color Online) Theoretical versus experimental solvation energies for ethanol, dimethyl ether (DME), propane (left to right): Joint Density Functional Theory as blue (gray) circles, zeroth-order diffusion Monte Carlo as black strikethrough x's, first-order corrected diffusion Monte Carlo as red (gray) x's. Experimental values from [7].

σ controls the transition width [62]. This description of water leads to the expression $A_{env}[n_{\mathrm{DFT}}] = \frac{1}{2}\int dr^3(n_{\mathrm{DFT}} - N)\left(\left(\frac{\nabla\cdot\epsilon(n_{\mathrm{DFT}})\nabla}{-4\pi}\right)^{-1} - \left(\frac{\nabla^2}{-4\pi}\right)^{-1}\right)(n_{\mathrm{DFT}} - N)$, where N represents the nuclei of the solute.

10^4 n_c (bohr^{-3})	3.0	5.0	7.0	8.1	9.0
dimethyl ether	9.0	7.8	7.0	6.7	6.5
ethanol	8.9	7.7	7.0	6.7	6.4
propane	10.3	8.9	8.0	7.7	7.5
acetone	10.6	9.2	8.3	8.0	7.7

Table 2.1: Formation energies (mH) for cavities at various values of the electron isodensity-contour parameter n_c from the model of Ref. [62], based on the cavitation energy method of Ref. [81].

2.5 Results.

Figure 2.1(b) shows the resulting solvation energies for acetone as a function of n_c. The results are not sensitive to σ, so we leave this value fixed at 0.6 and optimize the values of n_c for use in diffusion Monte Carlo. All of the variational Monte Carlo results and nearly all the diffusion Monte Carlo results lie below the density-functional theory data. The variational Monte Carlo results with no Jastrow factor (and thus no correlation, but exact exchange energy) and the diffusion Monte Carlo results lie very near to each other, indicating that the primary corrections in solvation energy to the density-functional results come from the exact treatment of the exchange and that corrections to correlation beyond the local-density approximation largely cancel for the solvation energies, at least for acetone.

A least squares fit of the data shown in Fig. 2.1b yields $n_c = 7.0 \times 10^{-4}$ bohr^{-3} as optimal for diffusion Monte Carlo and $n_c = 8.1 \times 10^{-4}$ bohr^{-3} as optimal for use with density-functional theory. Figure 2.2 shows the resulting solvation energies of three molecules for both the zeroth-order expression and the first-order corrected version from Eq. (2.3). The agreement between the quantum Monte Carlo results and experiment is encouraging given the particularly simple model employed here for the fluid. The figure also demonstrates the importance of using Eq. (2.3) to include the effects of self-

consistency, particularly for ethanol.

To estimate the remaining error between the corrected formula (Eq. (2.3)) and full self-consistency that could be achieved by following the steps in Figure 2.3, we employ two different electronic structure methods for which achievement of full self-consistency is feasible and whose difference in densities we expect to be similar to the density difference between density-functional theory and quantum Monte Carlo. We begin with an environment potential V_{env} from a solvated density-functional theory (Hartree-Fock) calculation, and include it in a Hartree Fock (density-functional theory) calculation, attempting to predict the final self-consistent energy using our proposed methods. Fig. 2.4 compares the zeroth and first-order corrected approximations with the fully self-consistent results when working this procedure in both directions.

The data exhibit a number of behaviors which we expect to be general trends. First, the first-order corrected data lie above the fully self-consistent result, regardless of the starting point. Second, the remaining (second-order and higher) errors are all quite small (0.2 mH or less) and on the order of about one-third the size of the first-order correction. Third, the remaining errors in the corrected results for a given molecule when going in either direction between density-functional theory and Hartree Fock are nearly identical. The difference between these remaining errors gives an estimate of the correction at odd orders (third and higher), indicating that the errors remaining are dominated by the second-order term. In aqueous solution, electrostatic screening, a negative-definite quantity, dominates this second-order term, thus explaining why the corrected results generally lie above the self-consistent solution.

These observations strongly suggest that the self-consistency error in our corrected diffusion Monte Carlo results is less than one mH for ethanol, and even less for the other molecules. Our procedure thus likely gives an upper bound well within chemical

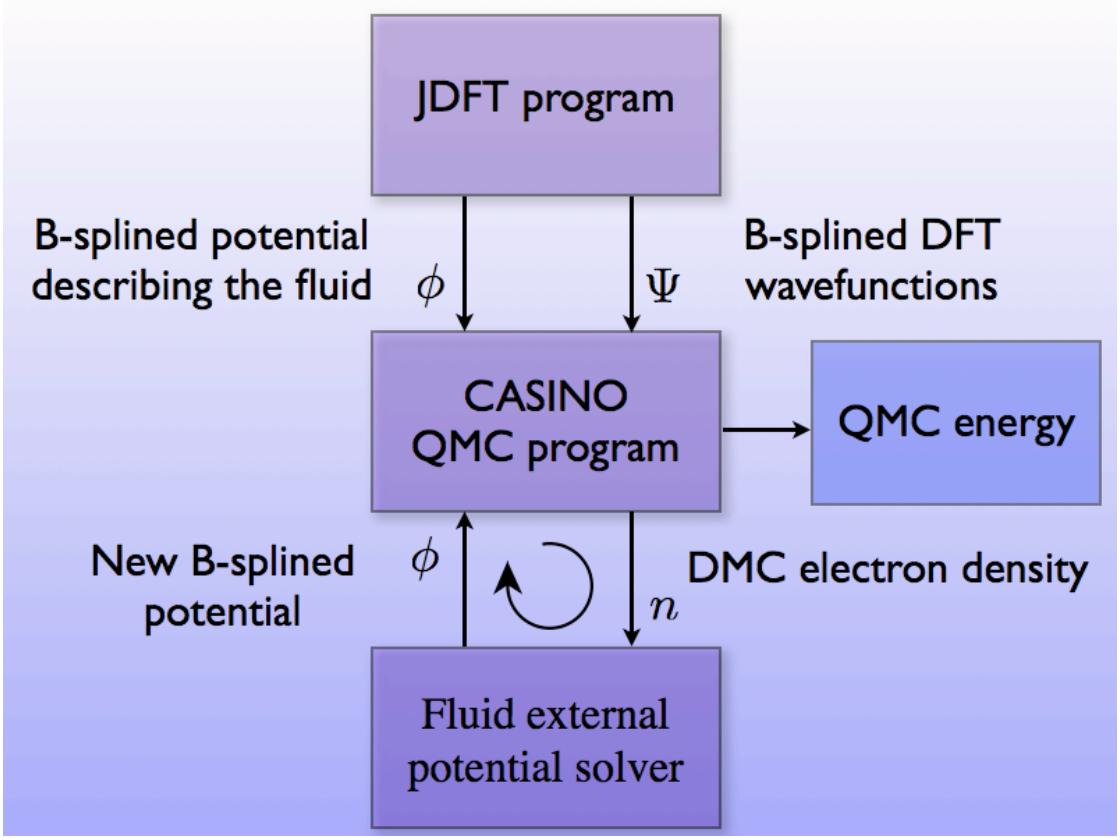

Figure 2.3: Alternate procedure for achieving self-consistency

accuracy of the results of full self-consistency, *with the need for only a single quantum Monte Carlo calculation*.

2.6 Conclusion.

The framework of joint density-functional theory provides a rigorous and efficient method for solvation in quantum Monte Carlo, without the need for phase-space sampling of the fluid. Moreover, a special procedure allows self-consistency of the joint calculation to be obtained (along with an estimate of the remaining errors) to within *chemical accuracy*, all at the cost of only a *single* quantum Monte Carlo total-energy

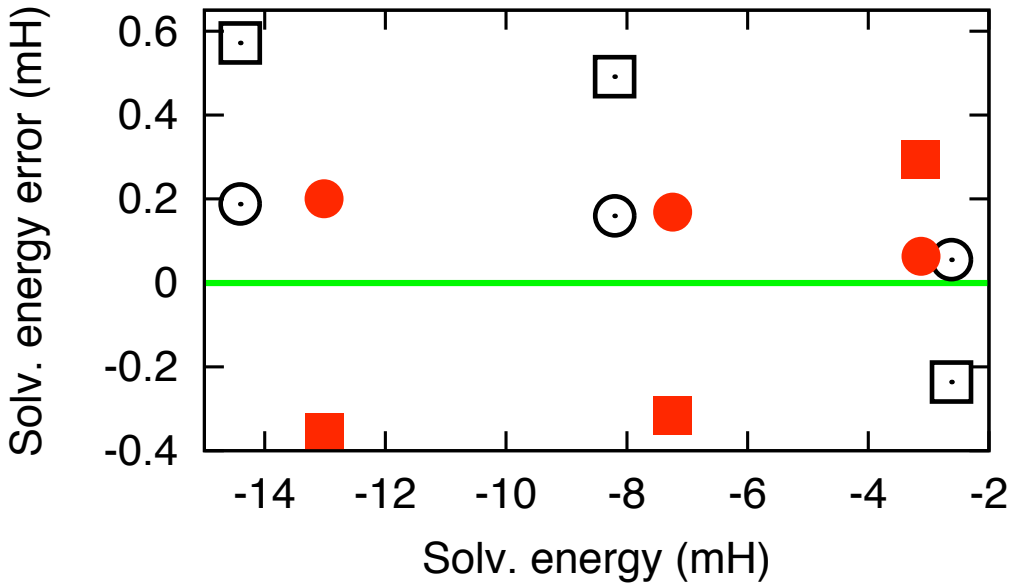

Figure 2.4: Zeroth order approximation errors (squares) and first order approximation errors from Eq. (2.3) (circles) relative to the exact self-consistent fluid-electronic structure minimization for Hartree-Fock calculations with LDA potentials in black (unfilled) and LDA calculations with Hartree-Fock potentials in red (gray) (filled), for the electrostatic solvation energies of ethanol, dimethyl ether, and propane (from left to right).

calculation carried out in a fixed external potential. This solvation method applies just as readily to molecular and surface calculations. The procedure is general and may be used not only with quantum Monte Carlo but other correlated total-energy methods as well.

2.7 Acknowledgements

Ravishankar Sundararaman helped with derivations and coding, Kendra Letchworth-Weaver helped with visualization and preliminary coding, and Tomas Arias co-wrote the

manuscript. Funding was provided by NSF Graduate Research Fellowships, CAREER DMR-1056587, DE-FG02-07ER46432, and desc0001086.

CHAPTER 3

LITHIUM SULFUR BATTERY MATERIALS, INVESTIGATED WITH DENSITY-FUNCTIONAL THEORY AND POLARIZABLE CONTINUUM METHODS

3.1 Introduction

Methods such as those described in the last section can be powerful tools for investigation of properties that are sensitive to electronic structure methods. However, these techniques are computationally expensive, and should be used for small systems and those where small energy differences are particularly important. The lithium-sulfur battery system is an experimentally and computationally complicated system, and much more computationally inexpensive techniques are needed to help identify what reactions and chemical species are relevant for battery operation. The theoretical and experimental challenges of lithium sulfur batteries include the equilibrium properties of lithium-sulfur mixtures, the kinetics of such mixtures (with and without applied voltage), and the spectroscopic identification of the resulting species and their concentrations.

This chapter uses density-functional theory to explore the equilibrium properties of lithium-sulfur mixtures and to examine the effect of dielectric constant and ionic strength on these equilibrium properties.

3.2 Sulfur Species Background

The basic lithium-sulfur battery contains a lithium anode, a cathode containing sulfur, and an electrolyte composed of an aprotic solvent with dissolved salt. As the battery

operates, the sulfur is reduced and a number of anionic sulfur species are formed and then reduced, ultimately to form lithium sulfide, LiS_2. The exact mechanism leading to the formation of LiS_2 is unknown, although certain sulfur anions have been spectroscopically observed during battery operation.

Sulfur anions are key components of lithium-sulfur batteries, and despite the extensive literature on sulfur anions, their structures and equilbria and not completely understood. Sulfur anions are present in the solid state as salts of alkali and alkali-earth metals, and in solutions in equilibrium with multiple anionic sulfur species. Because of the complex equilibrium and the fact that the anions are highly reactive in both oxygen and water, their properties are still debated [77]. However, a set of the sulfur anions are relatively well-characterized, due to their unique spectroscopic properties.

Lithium-sulfur battery studies frequently involve the reduction of elemental sulfur, S_8, which exists in solid form as stacked rings. Under reducing conditions, the S_8 reacts with two electrons to become S_8^{2-}, and a ring opening reaction occurs [44]. The linearized structure's global minimum appears to be a helical chain, although a number of different conformers may also be present in equilibrium with the helical form [27]. Other sulfur anions are subsequently produced, most notibly S_3^{1-}, best known for its intense blue color and large 620 nm peak in visible spectroscopy. S_3^{1-} also is known to equilibrate with S_6^{2-} [77]. These shorter sulfur anion species have fewer local minima, with the helical chain isomer being most dominant species [27]. Other sulfur anions are most likely present in these experiments, but the ratios of these species are highly influenced by the solution conditions.

The solvent plays a large role in the equilibrium behavior of the sulfur anions, yet experiments use a wide variety of solvents and added salts despite the fact the solvent is known to change key reactions [34]. One study examined eighty-five papers, and

found eight different categories of solvents that have been used in lithium-sulfur publications [27], ranging from tetraethylene glycol dimethyl ether [6], with a dielectric constant ~7, to DMF [28], to DMS [37], with a dielectric constant ~47.

Ab initio work to date has focused on spectroscopic identification of the many sulfur anion species, although the accuracy of the chosen methods is a source of concern. To obtain converged results, calculations for raman frequencies, optical spectra, and x-ray spectra all require better basis sets than calculations of ground-state energies. Additionally, such calculations need careful benchmarking against known standards to ensure that they produce accurate results. This is problematic because the sulfur anions exist in solutions in a complex equilibrium, and isolated standards are not available.

This chapter introduces an entirely different approach that circumvents these problems: using solution free energies and statistical mechanics to determine the thermodynamic properties of the idealized electrochemical system, corresponding to a voltage sweep rate of essentially zero so that kinetic barriers are not relevant. This study is limited to the solvated sulfur anions and S_8, and insolubility, bulk phases, and lithium-bound species are not considered here. Additionally, vibrational effects are not considered here. This scheme enables prediction of the extant sulfur species under varying experimental conditions, including varying the dielectric constant of the electrolyte. Moreover, this approach allows creation of idealized voltammograms, with the trends in peak placement in good agreement with experimental voltammograms, thereby simplifying the interpretation of the experiments.

3.3 Equilibrium Studies

While the species present in battery systems may still be debated, experimentalists can develop electrochemical systems with more defined conditions to create benchmarks for species identification. The simple experimental setups considered here contain low, well-measured concentrations of lithium and sulfur, from lithium sulfide and elemental sulfur. The species are solvated in dimethylformamide or tetraglyme, without additional salt. Low concentrations of sulfur species and lack of salt are necessary conditions so that the solutions remain as ideal electrolytes, with no Debye-Huckel effects complicating the analysis of the theory and experiments. To go beyond this, this chapter briefly considers *ab initio* calculations performed in ionic solutions, which the results demonstrating that the geometries of the species are very sensitive to the solvent conditions and require geometry optimization in ionic solutions. Such optimization is currently not available in the software package utilized here, and thus beyond the scope of this work.

Using the grand canonical ensemble, the net sulfur and sulfur-charge concentrations take the form

$$\bar{S}_{tot} = \sum_i \bar{N}_i S_i \tag{3.1}$$

$$\bar{Q}_{tot} = \sum_i \bar{N}_i Q_i, \tag{3.2}$$

where S_i is the number of sulfur atoms in the given sulfur species, N_i is the concentration of that species, Q_i is the charge of that species, S_{tot} is the total concentration of sulfur, and Q_{tot} is the total sulfur charge, which must also be equivalent to the lithium concentration.

Next, to determine the needed concentrations, we employ the grand partition func-

tion,

$$\mathcal{Z} = \prod_i e^{-\beta N_i (E_i - S_i \mu_s - Q_i \mu_Q)} \tag{3.3}$$

where the β is the standard inverse temperature $1/(k_B T)$, μ_S is the sulfur chemical potential and μ_Q is the chemical potential of the negative charge, ultimately corresponding to electrode potential. Differential of the the partition function then yield the total concentration of sulfur, the total lithium concentration, and the concentrations of each of the sulfur species in the form

$$-\frac{\partial lnZ}{\partial(\beta\mu_S)} = \bar{S}_{tot} \tag{3.4}$$

$$-\frac{\partial lnZ}{\partial(\beta\mu_Q)} = \bar{Q}_{tot} \tag{3.5}$$

$$-\frac{\partial lnZ}{\partial(\beta E_i)} = \bar{N}_i. \tag{3.6}$$

To determine the chemical potentials for given net sulfur and lithium concentrations, one solves (3.4-3.5), we here employ two nested bisection solves. With the chemical potentials then in hand, (3.6) gives the concentration of each species.

3.3.1 Results and Discussion

Figures 3.1 and 3.2 demonstrate the equilibrium concentrations of sulfur anions predicted for lithium to sulfur ratios ranging from 1:4 to 2:1, in a solvent of low ($\epsilon = 7.58$) and high ($\epsilon = 37$) dielectric constant, respectively. The figure orders the anions from top down by increasing charge per sulfur atom, considering mono- and di-anions from S_8 to S, as well as the neutral species S_8. The results demonstrate that at low lithium ratios, the low-charge per sulfur species are present, whereas at high lithium ratios, the high-charge per sulfur species are preferred. Additionally, both the theoretical predictions and the experiments identify S_3^{-1} as an important species, and species such as S_7^{2-} as not relevant.

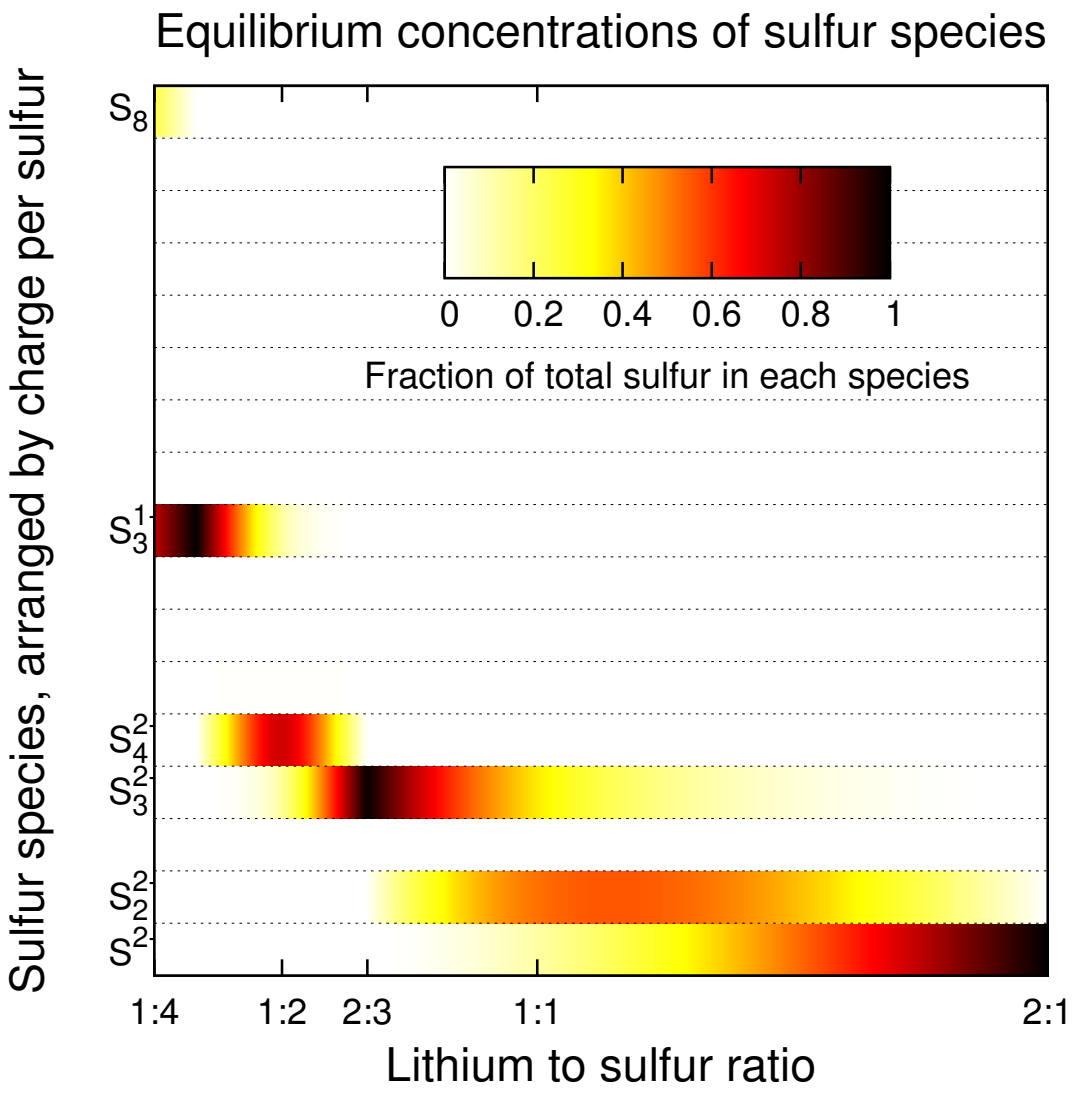

Figure 3.1: Calculated sulfur species concentrations for different lithium to sulfur ratios, for 1 μM sulfur solutions, with lithium concentrations ranging from 0.25 to 2 μM, from one thousand equilibrium calculations. One can see that species with low charge per sulfur exist at the low lithium to sulfur ratios, and that as the ratio increases, the higher-charge sulfur species become preferred. The dielectric constant is set to $\epsilon = 7.58$ here, for THF, for instance.

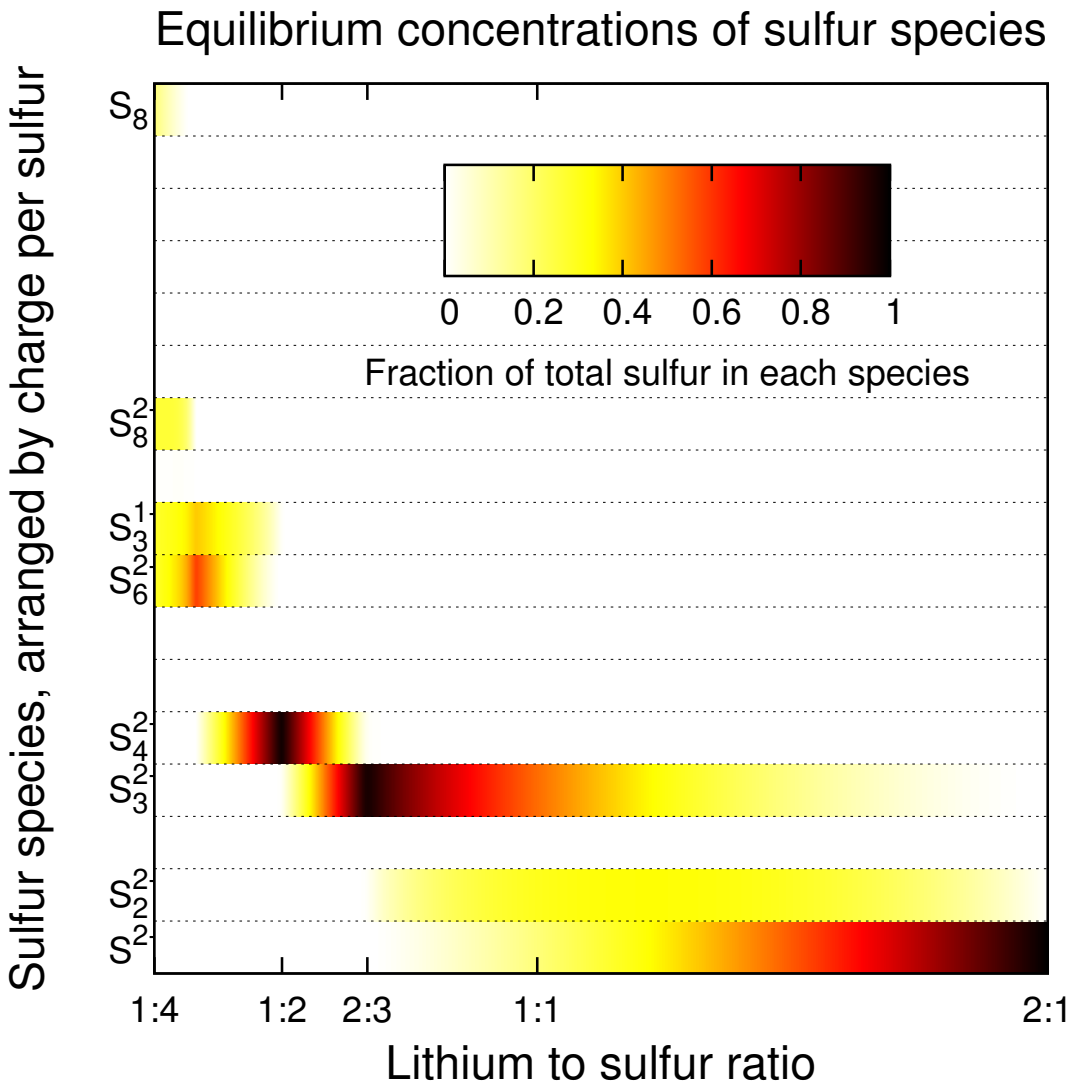

Figure 3.2: Predicted sulfur species for different lithium to sulfur ratios, using the same conventions as Figure 3.1 but for a solvent with dielectric constant $\epsilon = 37$ such as, for instance dimethylformamide or acetonitrile.

The dielectric constant also plays a role in determining the species present. From examination of a low lithium to sulfur ratio, one can see that the equilibrium: $S_3^{1-} \rightleftharpoons S_6^{2-}$ is shifted to the right as the dielectric constant increases. This is an important finding because S_3^{-1} appears as a strong spectroscopic peak in both UV-Vis spectroscopy and electron spin resonance, so understanding the behavior of the S_3^{1-} is a priority for experimentalists. On the high lithium to sulfur ratio side, one can see that at the higher dielectric constant, S_3^{2-} is more stable than at lower dielectric constant, where S_2^{2-} is relatively more stable.

Voltages at which key oxidations occur are needed to more directly compare the calculated results to experiments. Fortunately, the grand-canonical calculations include not only the equilibrium concentrations of the sulfur species, but also the electron chemical potentials at which the various sulfur species oxidize and reduce. These values are obtained solely from the species solvated free-energy values E_i from the *ab initio* calculations, and equation 3.3. Figures 3.3 and 3.4 show the resulting voltammograms and integrated charge plots for the two dielectric constants we have considered ($\epsilon = 7.58$, $\epsilon = 37$). The increase in dielectric constant shifts the peaks towards higher voltage. Inclusion of ionic effects should also shift the peaks to the right, so these voltages are not expected to be exactly comparable to experimental results.

Our results, being based on thermodynamic equilibrium do not take kinetics into account and thus represent idealized voltammograms taken at essentially infinitely slow sweep rates. The results, however, do give insights as to possible reaction mechanisms, as they identify the species present at different voltages which may serve as possible intermediates. S_2^{2-}, for instance, is predicted to exist around -2.7 V (vs. Ag/Ag^+) in triglyme, and so could be involved in S^{2-} oxidation.

The experimental situation is that lithium-sulfur voltammograms contain two main

reduction peaks, with the exact reactions happening at these peaks remaining an area of active research. Some experiments [28, 22] have observed S_8^{2-} and S_3^- at the first peak in the Li-S voltammogram, using an electrolyte containing dimethylformamide, in concurrence with our *ab initio* predictions.

A more full look at the experimental literature, however, reveals that studies attempting to identify the species present at different points in the reduction process are not yet in agreement with each other. The sulfur anions identified in various studies are depicted in Table 3.3.1. In dimethylformamide, one study [43] concludes that S_n^{2-} and S_n^{1-} are involved, where n = 3,4,6,8, and another study [28] concludes that S_8^{2-}, S_3^{1-}, and S_4^{2-} are produced during the first wave, and the second wave includes the production of S_7^{2-}, S_6^{2-}, S_5^{2-}, S_4^{2-}, S_3^{2-}, S_2^{2-}, S^{2-}. However, a study in dimethyl sulfoxide solutions [37] predicts that S_8^{2-}, S_6^{2-}, S_4^{2-}, S_3^{2-}, and S_3^{1-} are produced at the first wave, and S_8^{4-}, S_3^{2-}, and S_4^{2-} are also produced in the second wave. The solvent used in that study has a dielectric constant of $\epsilon = 47$.

A more recent paper, [6], however, is more in line with our results, albeit for a different dielectric constant. This experiment was performed in triglyme ($\epsilon = 7.58$) with the addition of salt, but very nearly matches our results for DMF ($\epsilon = 37$) with no included ionic effects, for reactions occurring with the larger sulfur species. The ionic effects from the salt appear to be very important, and mimic the effects of higher dielectric constant. Reference [6] argues that the first reduction step is at 2.4-2.2 V vs Li^+/Li (or about -1 to -1.2 V vs. Ag/Ag^+), and produces S_8^{2-} and S_6^{2-}, and S_3^{1-} is also present. I observe this identical peak, with the same reaction products. The second reduction step is at 2.15-2.1 V vs Li^+/Li (or about -1.2 to -1.3 V vs. Ag/Ag^+), producing S_4^{2-}, and a reduction between 2.1 V and 1.9 V vs. Li^+/Li leads to S_3^{2-}, S_2^{2-}, and S^{2-}. I find a second reduction step to be somewhat shifted, at -1.4 V vs. Ag/Ag^+, and the last

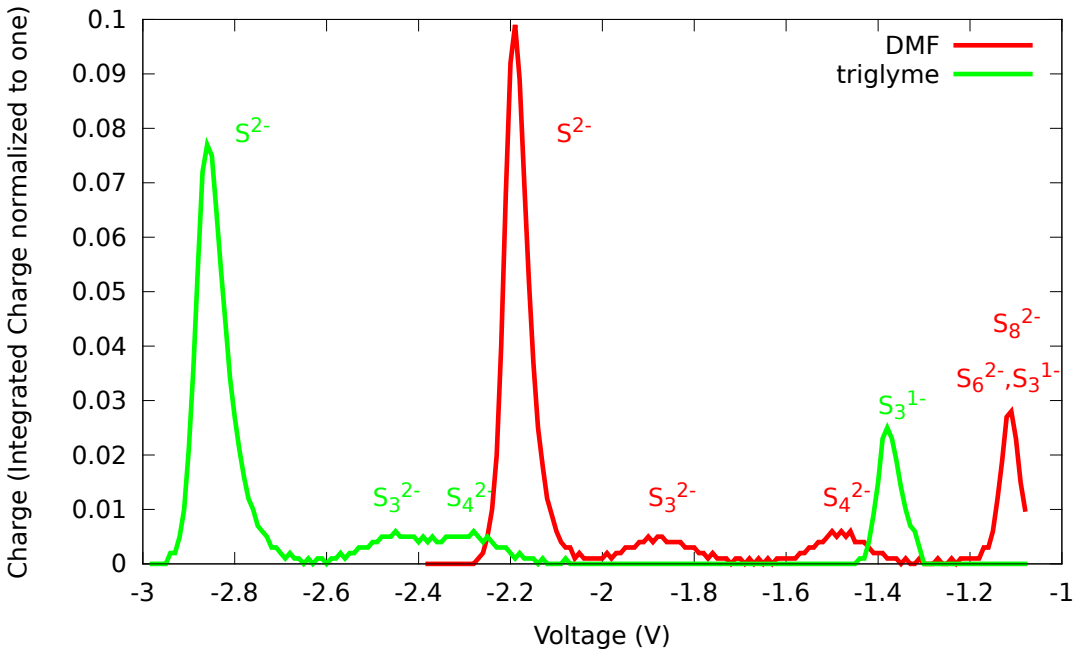

Figure 3.3: Voltammogram with voltage relative to Ag/Ag^+, showing the discharge of the idealized battery with a sulfur electrode.

reduction step to be even further to the right of the experimentally predicted voltage, but the trends and ordering of reduced species match these experimental results exactly. The good agreement between my work and this study suggests that for some of the sulfur reduction and oxidation processes, the thermodynamic effects are most important, and not all of the reaction the processes are necessarily kinetically controlled.

The dielectric constant of the solution strongly affects the equilibrium properties of the sulfur solutions, but the ionic properties must also be considered, especially because typical experimental conditions include added salts. Because the ionic model in Gaussian does not allow for geometry optimization, preliminary calculations to assess the importance of geometry relaxation were performed using optimized geometries from the non-ionic calculations using the two different dielectric constants. The results were drastically different depending on the choice of geometry for the species. Figures 3.6

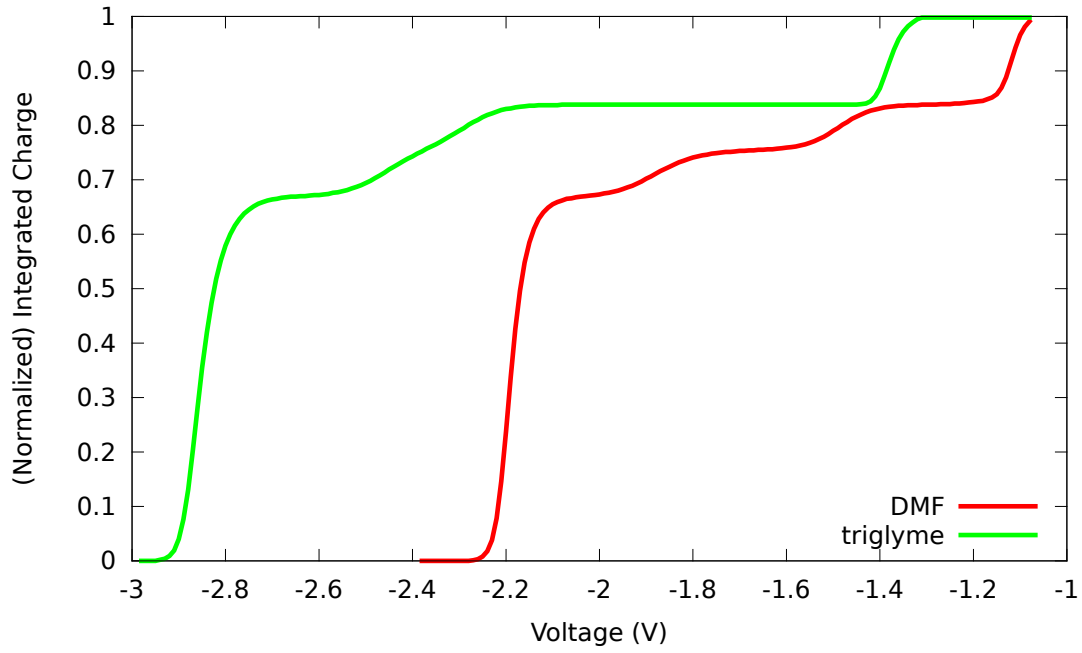

Figure 3.4: Integrated charge plot showing the discharge of the idealized battery with a sulfur electrode.

and 3.7 demonstrate calculations at a dielectric constant of 7.58 using the optimized geometries for calculations using a dielectric constant of 7.58, and with 37, respectively.

The results clearly indicate that the energies of the species are highly influenced by these geometry changes. For reliable results, the species must have geometry optimization performed in the ionic solutions. For example, in these preliminary calculations, S_2 was erroneously found to be more stable than S_8. In comparison, the calculations without ionic effects do not predict that the S_2 is more stable than the S_8. This further reinforces the conclusion that geometry optimization in ionic solutions is important for these charged species.

Solvent	THF	TEGDME	DMF			DMSO
Dielectric Constant	7.58	7.9	37			47
Reference	this work	[6]	this work	[43]	[28]	[37]
S_8	X	X	X	X	X	X
S_8^{1-}				X		
S_7^{1-}						
S_6^{1-}				X		
S_5^{1-}						
S_4^{1-}				X		
S_8^{2-}		X	X	X	X	X
S_7^{2-}					X	
S_3^{1-}	X	X	X	X	X	X
S_6^{2-}		X	X	X	X	X
S_5^{2-}					X	
S_2^{1-}						
S_4^{2-}	X	X	X	X	X	X
S_3^{2-}	X	X	X	X	X	X
S^{1-}						
S_2^{2-}	X	X	X	X	X	
S^{2-}	X	X	X		X	

Table 3.1: Comparison of sulfur species identified in lithium-sulfur experiments and in this work, where THF is tetrahydrofuran, TEGDME is Tetraethylene glycol dimethyl ether, DMF is dimethylformamide, and DMSO is dimethyl sulfoxide.

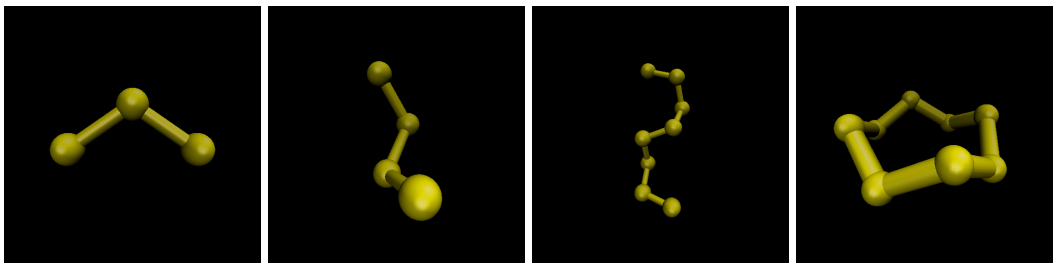

Figure 3.5: Representative sulfur species, from left to right, S_3^{2-}, S_4^{2-},S_8^{2-}, and S_8. The S_8 is the only cyclic species- all others are twisted (helical) chains. The bond lengths for nearest neighbor sulfur atoms for all 4 species are 2.1 angstroms.

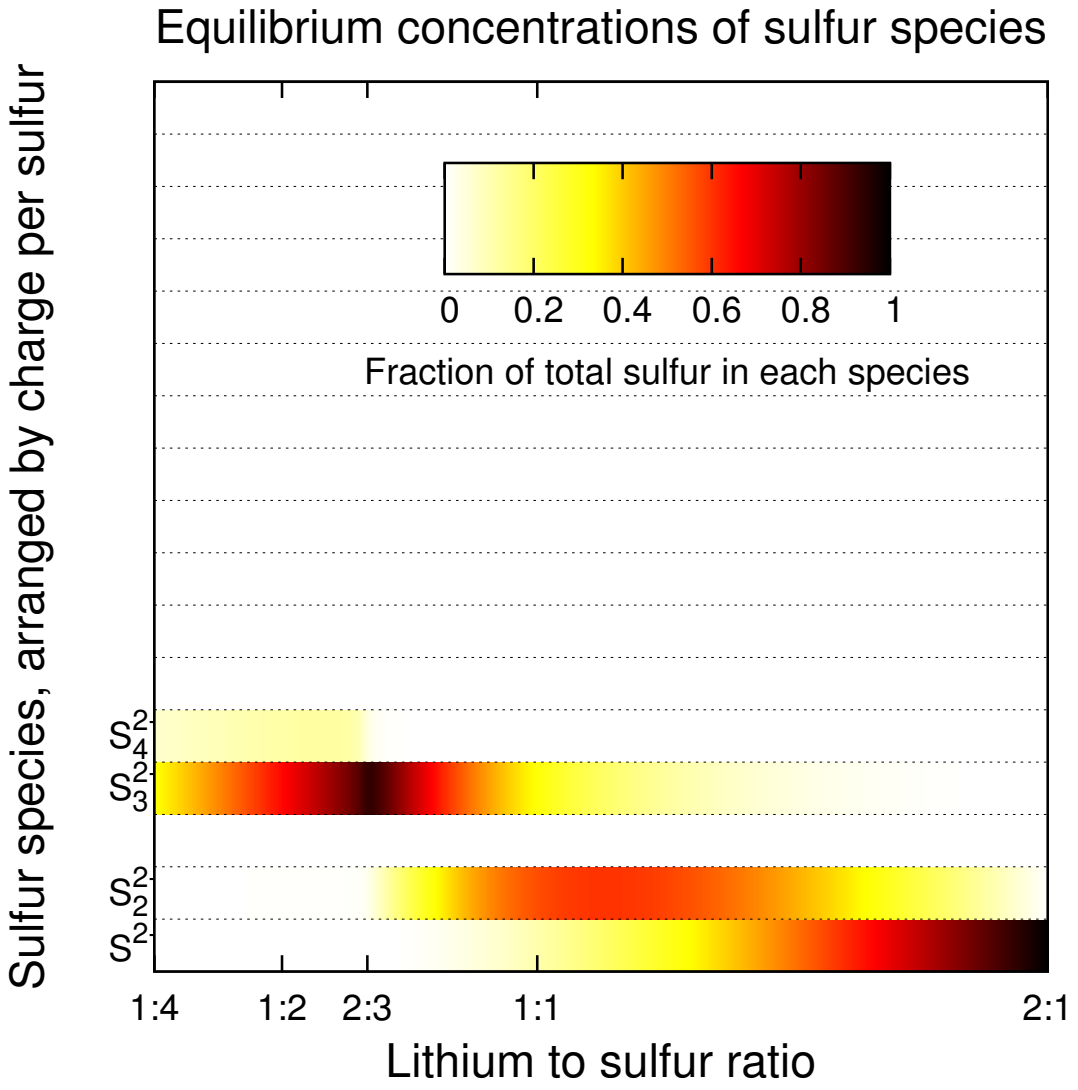

Figure 3.6: Predicted sulfur species at equilibrium in an ionic solution with a dielectric constant of 7.58, with geometry optimization using a dielectric constant of 7.58, but with no ionic screening. The species most stable on the far lefthand side of the plot is S_9^{2-}, which is not shown.

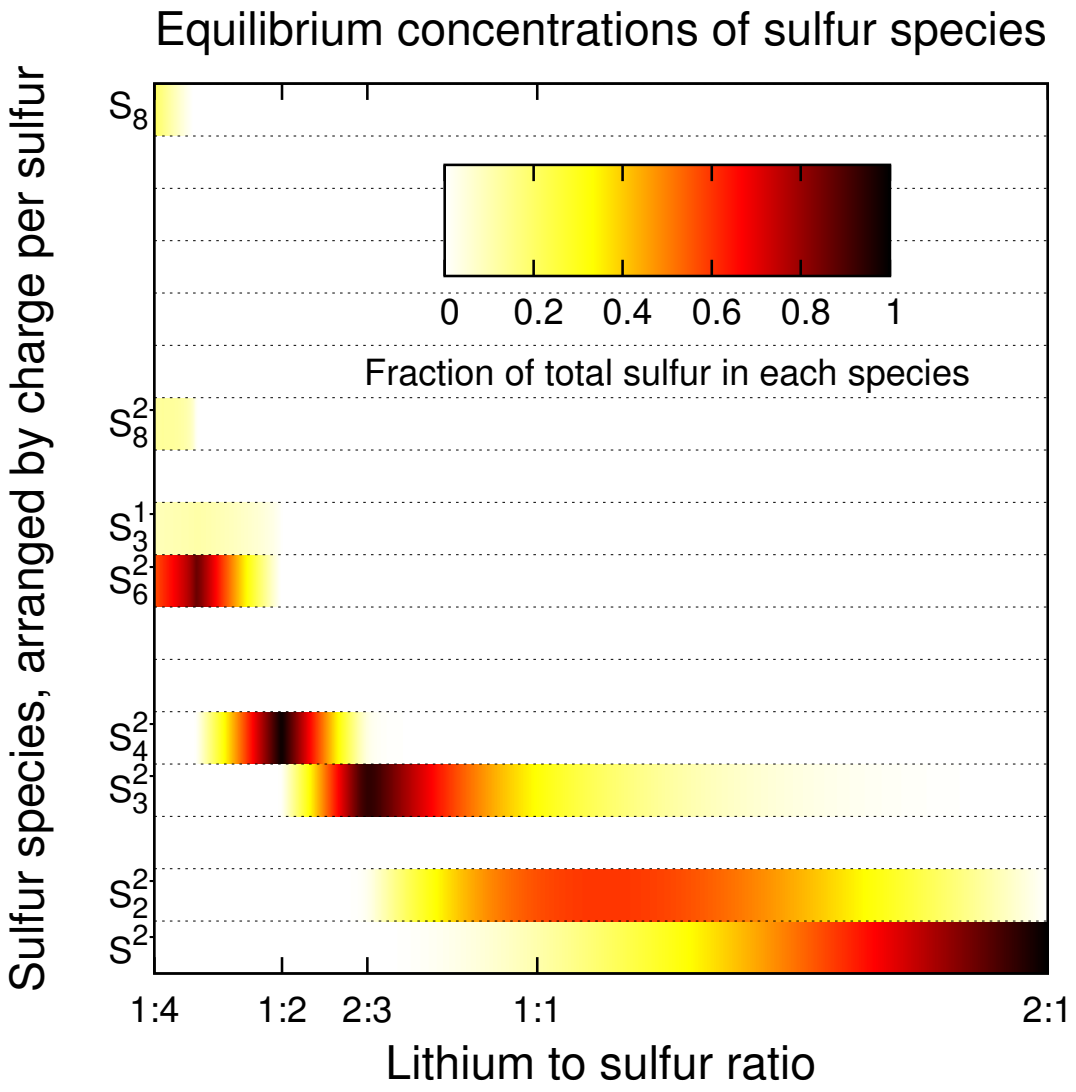

Figure 3.7: Predicted sulfur species at equilibrium in an ionic solution with a dielectric constant of 7.58, with geometry optimization using a dielectric constant of 37, but no ionic screening.

3.3.2 Calculation Details

The calculations were performed in the Gaussian code [21]. All structures were optimized and energy values were calculated with the same basis and level of theory, chosen here to be a hybrid density-functional calculation with the B3LYP functional. The energies were computed with the Gaussian basis set 6-311++G(2df), and with the polarizable continuum model using a dielectric constant of 7.58 (and 37 for Figure 3.2), and with the Gaussian program parameters for tetrahydrofuran. The cavity size was kept constant as the dielectric constant was varied for two reasons. Firstly, because the continuum fluid represents an idealized fluid, and can represent a variety of solvents. For instance, both acetonitrile and dimethylformamide have dielectric constants ~37. Secondly, if the cavity size was altered, the effect of the dielectric constant would no longer be clear. Geometries optimized in the solvent with a dielectric constant of 37 are provided as Gaussian input files in the appendix.

3.3.3 Conclusions

The *ab initio* calculations and equilibrium studies performed here provide insight into the complexities of the lithium-sulfur system, and provide a natural pathway forward for further exploring this system. The results provide perfect resolution to the voltammograms, providing information as to the exact species responsible for each peak in the idealized voltammograms, unlike in experiment, where the species cannot be automatically identified. Additionally, the results are in better agreement with more current experimental work [6], suggesting that experimental progress towards identifying sulfur species is improving, but could still benefit from the guidance of careful computational work.

However, the realities of the electrochemical experiments may not be completely captured by this work, and a careful examination of these factors must be considered. Firstly, it is possible that species other than those considered could be important in experiments. While the sulfur anions as large as S_8^{2-} and S_8^{1-} were considered here, if disproportionation reactions are very important, it is not impossible that even larger sulfur anions are present. However, based on the trend of decreasing size of sulfur anion as the voltage sweeps downwards, one would not expect this to impact the results after the first peak. Given that S_8^{2-} is experimentally observed, the argument is weak for larger sulfur anions as important species for the experimental voltammogram. Additional geometries for the sulfur species could also be considered. This is possibly important if multiple configurations of the anions are present in solution, a concern for the larger sulfur anions such as S_8^{2-}. However, once again, this is not expected to qualitatively change the results, given that S_8^{2-} is only present at the first peak in the voltammogram. The geometries of the smaller sulfur species are less likely to have multiple configurations, and their geometries are well-known in the sulfur anion literature. Other errors could be present as a result of using continuum solvation, the use of density functional theory, and the assumption that zero-point energy contributions are insignificant. These errors are more difficult to assess, although the agreement in peak position with experiment suggests that these errors may not significantly change the results.

This study has established that idealized voltammograms can contribute towards the understanding of experimental lithium-sulfur battery systems, and subsequent work can now naturally progress towards introducing more experimental complications into the calculations to bridge the gap between the theory and the experiments.

The results indicate that the ionic nature of the electrolyte is important- further work should investigate geometries of the sulfur species optimized in ionic solvents. This is

not unexpected for the sulfur anions, as they are highly charged and would be expected to undergo changes in configuration as screening is introduced.

Another experimental complication is that the lithium may not be dissociated from the sulfur anions. The calculations assume that the lithium is dissociated from all of the sulfur anions, but the experimental reality may be that some fraction of some of the sulfur anions have lithium cations attached. This would be expected to be most important for the sulfur anions with a higher charge-per-sulfur ratio. Future studies could account for this for species such as LiS^-, by including the energy of this species and a chemical potential for the lithium. The lithium-sulfur dissociation is related to another complication in the experiment, that some of the sulfur species may be insoluble. This could complicate the experimental voltammograms, whereas here, the species were assumed to be soluble.

Lastly, these calculations assume that the sulfur species are able to reach equilibrium, which may not be the case depending on the timescales of the experiments. This is difficult to address because these calculations assume thermodynamic equilibrium, and do not make any assumptions about reaction mechanisms. However, one can speculate about reaction mechanisms by using these voltammograms, and identifying species that are expected to be present at each voltage. Combining this knowledge with experimental knowledge could lead to new insights on the reaction mechanisms.

3.4 Acknowledgments

Michael Lowe provided useful discussions and initial geometries for many of the sulfur species, which were further optimized, and in some cases, independently found. Ravishankar Sundararaman providing coding advice and useful discussion.

CHAPTER 4

TIME DEPENDENT DENSITY-FUNCTIONAL THEORY FOR IDENTIFYING AND CHARACTERIZING DEFECTS IN PENTACENE THIN FILMS

4.1 Introduction

Solvation models used to describe liquids may provide a reasonable starting point for the approximation of the electronic environment of molecular crystals. This chapter[1] explores the practice of applying a polarizable continuum solvation model to describe the solid environment in a pentacene crystal. Here, the continuum solvation approximation allowed for a sufficiently accurate description of the pentacene crystal [48] that calculations of spectroscopic properties of defects were able to be used to predict the identify a defect, which was subsequently observed in experiments [75].

Organic semiconductors are attractive materials for microelectronic and photovoltaic applications because their energy levels, optical properties, and solubility can be adjusted through the inclusion of functional groups. While significant progress towards the commercialization of organic semiconductor devices has been made, the long-term reliability of most organic semiconductors remains a concern. Charge trapping, for example, causes a wide array of functional problems in organic semiconductor devices including a reduction in mobility, an increase in off-current, and an increase in operating voltage. Yet trap formation in these materials remains poorly understood, even in pentacene, the most widely studied organic semiconductor. Proposed trapping mechanisms in pentacene include the immobilization of charge at grain boundary defects [68, 49] and dielectric interfaces, [49, 89, 40] formation of immobile bipolarons, [78] and chemical re-

[1] Figures and portions of written content in this chapter reprinted with permission from [48], Copyright 2011, WILEY-VCH Verlag GmbH and Co. KGaA,Weinheim

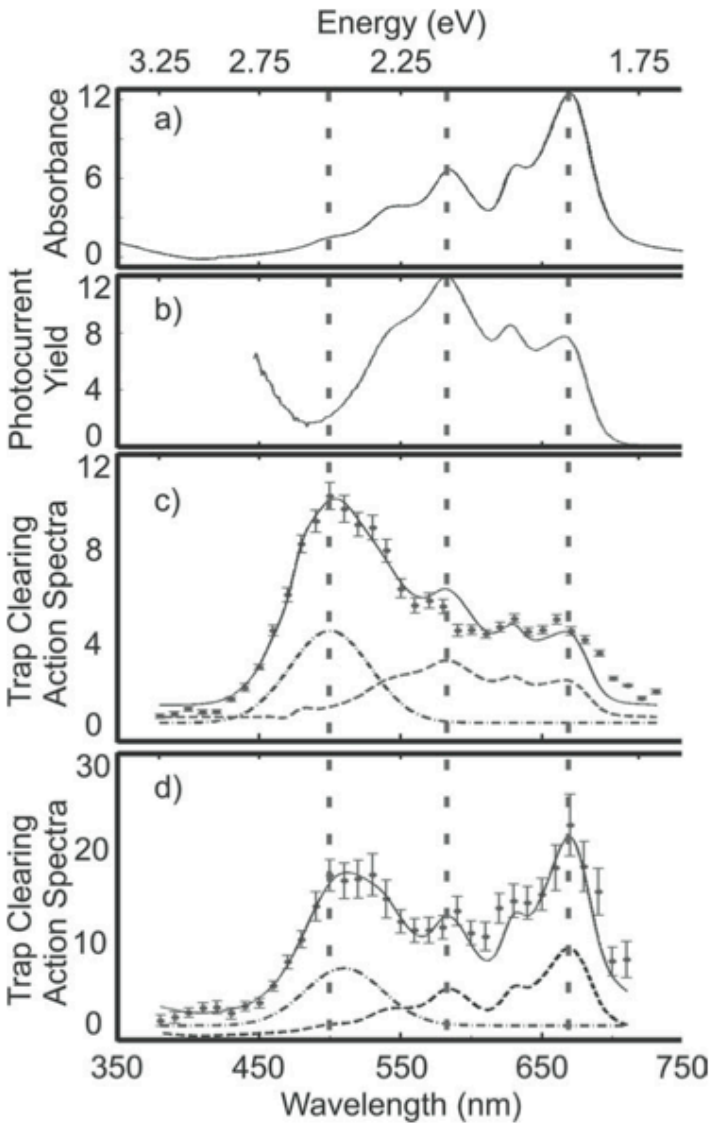

Figure 4.1: a) Experimental absorbance (scale: arbitrary units) and b) photocurrent yield [11] of bulk pentacene (scale: 10^{-4}). Experimental trap-clearing action spectrum acquired at two locations of the pentacene film (circles; scale: 10^{-3} eV^{-1} s^{-1}). The solid line in (c) is a fit to a linear combination of the photocurrent spectrum (dashed line) and a Gaussian (dash-dotted line; center = 2.48 eV, width = 0.14 eV). The solid line in (d) is a fit to the absorption spectrum (dashed line) plus a Gaussian (dash-dotted line; center = 2.43 eV, width = 0.13 eV).

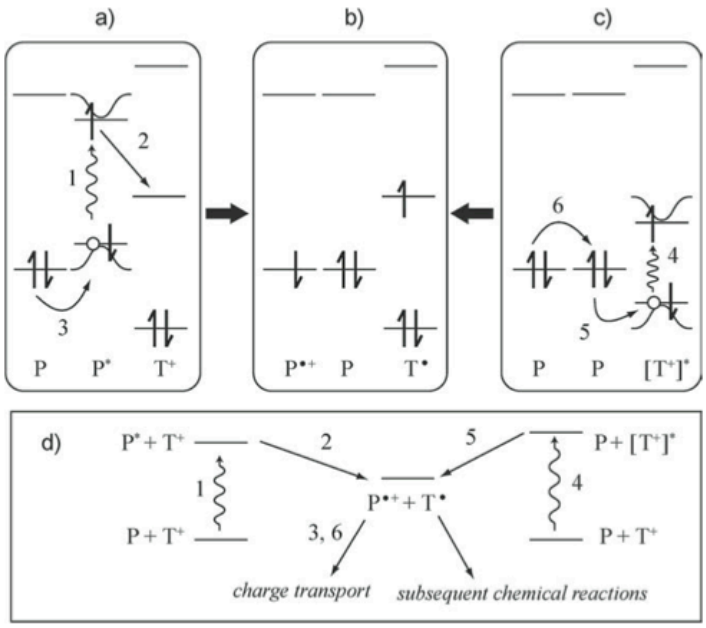

Figure 4.2: Trap-clearing mechanisms. Here P indicates pentacene, P^* is photoexcited pentacene, and $P^{\bullet+}$ is the pentacene cation radical. The trapped species appears as: a neutral radical, $T^\bullet$; charged, T^+; or photoexcited and charged, $[T^+]^*$. In (a), a pentacene molecule near a charged trap absorbs light (step 1). Trap-assisted exciton splitting (step 2) populates the trap with an electron and puts a hole onto pentacene, which may be converted to a free hole via charge transfer to a distal pentacene (step 3) to yield the charge-liberated configuration shown in (b). In (c), the cationic trap species is photoexcited directly (step 4) and the trapped hole is released via electron transfer from an adjacent pentacene (step 5). Charge transfer to a distal pentacene (step 6) yields configuration (b). Both trap-clearing mechanisms are summarized in the state diagram in (d).

actions. [57, 50, 41, 39] Many transistor studies indicate a degradation of device performance following exposure to air, moisture, and/or light, [95, 63, 50, 59, 51, 25, 93, 39] but whether this degradation arises from physisorbtion [95, 63, 51, 25] or a chemical reaction [57, 50, 41, 93, 39] remains an open question. Although optical absorption [50] and recent X-ray photoelectron spectroscopy [90, 93] studies have provided more definitive evidence of chemical transformations in aged transistor films, the relationship between the observed reaction products and trapped species remains unclear.

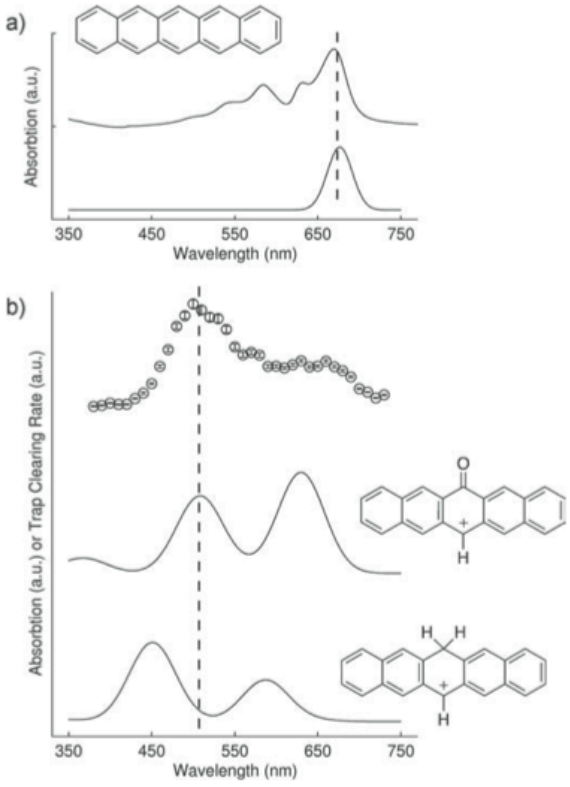

Figure 4.3: Measured and predicted spectra. a) Pentacene absorption spectrum: measured (upper solid line) and calculated (lower solid line). The calculated spectrum was broadened by 15 nm. b) Measured trap — clearing spectrum (upper solid circles with error bars) and the calculated absorption spectrum for the charged oxygen defect (middle line) and the charged hydrogen defect (lower line). The middle and lower curves were generated by broadening the calculated absorption spectra by 28 nm. The dotted vertical lines are a guide to the eye.

In this chapter, I show the calculated optical spectra of candidate trapping species, and compare these results with experimental data from a new spectroscopic method for microscopically probing the electronic states of long-lived trapped charged species in a π-conjugated film. Pentacene's small size allows one to carry out quantum chemical calculations, which are compared to experiment. Traps in pentacene and a wide-variety of organic semiconductors exhibit a similar 0.6 eV activation energy and, it has been suggested, may therefore share a common trapping mechanism. [51] Our results pro-

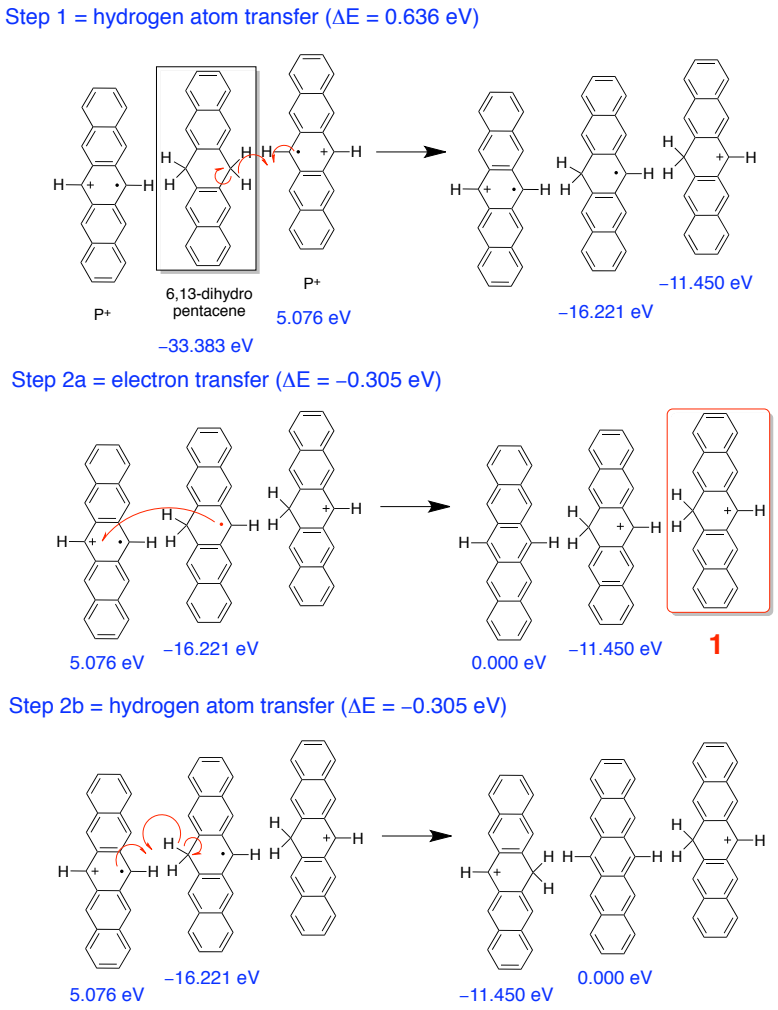

Figure 4.4: Chemical reaction of 6,13-dihydropentacene with two pentacene cations to yield the trap species 1 (red). Energies, shown in blue, were calculated using density-functional theory as described in the text. The energies are shown in units of electron volts relative to pentacenes ground state energy (-31.1268 Hartree= -847.002 eV). We predict a reaction energy of ΔE = +0.331 eV.

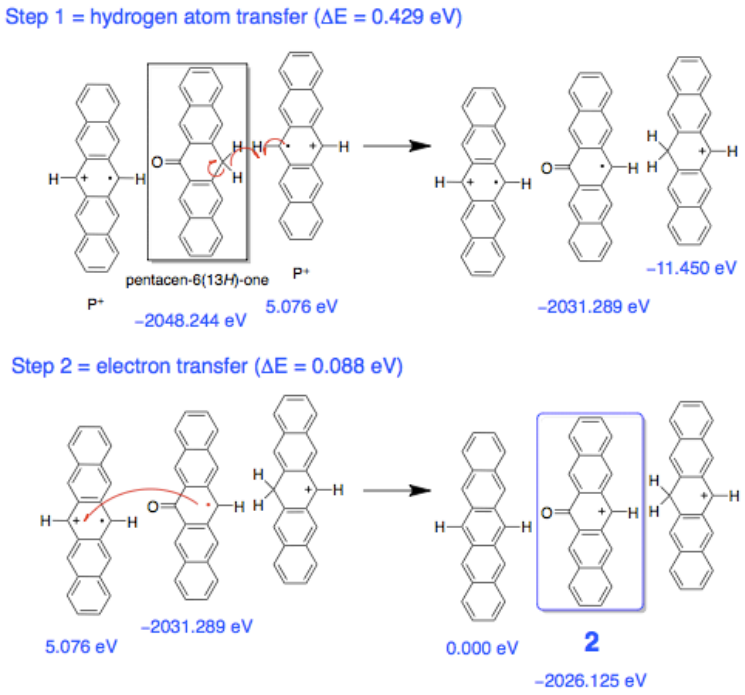

Figure 4.5: Chemical reaction of pentacen-6(13H)-one with two pentacene cations to yield the trap species 2 (blue). Energies, shown in blue, were calculated using density-functional theory as described in the text. The energies are shown in units of electron volts relative to pentacene's ground state energy (-31.1268 Hartree = -847.002 eV). I predict a reaction energy of ΔE = +0.517 eV.

vide spectroscopic evidence for pentacen-6(13H)-one as the most likely trap species in pentacene. Because polyacenes such as pentacene are promising candidates for field-effect transistors [45, 3, 79, 31] and solar cells, [94] this finding should be of general interest to the organic electronics community.

The clearing of trapped positive charge by light in organic semiconductors is usually attributed to the recombination of trapped holes with excitons, [70] free electrons, [70] or bipolarons. [78] The observation of light-induced trap clearing is usually taken as evidence against trapping due to migration of charge into the dielectric. [69, 49] In the excitonic trap-clearing mechanism sketched in Figure 4.2a, light is absorbed to create an

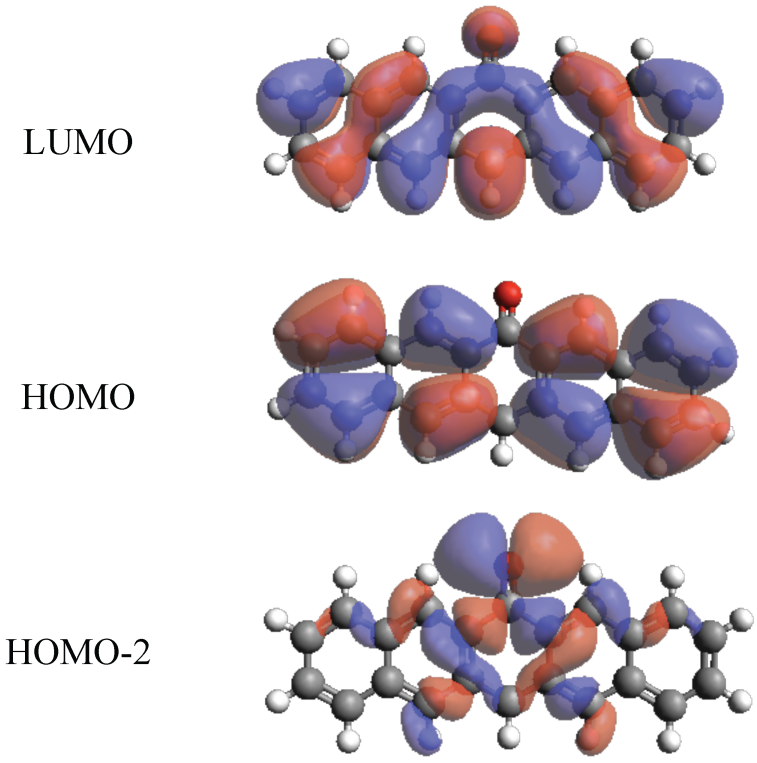

Figure 4.6: Selected defect 2 orbitals.

exciton (step 1), the excited electron is transferred to an unoccupied state at the trap site (step 2), and the excited hole relaxes and percolates away via electron transfers between adjacent pentacene molecules (step 3). The mid-gap state at the T^+ site in Figure 4.2a could be a state associated with a grain boundary, [68] a sliding defect, [36] or a valence orbital in pentacene stabilized by dipoles in the nearby dielectric. [89, 40] Consistent with the mechanism of Figure 4.2a, light-enhanced trap clearing was observed at wavelengths where absorption creates either an exciton localized over a single molecule [33] (at 630 nm and 675 nm) or a charge-transfer exciton with intermolecular character [72] (at 575 nm).

In addition to these expected spectral features, the trap-clearing action spectra of Figure 4.1c,d exhibit a large peak near the wavelength λ =500 nm (photon energy). This finding is surprising for two reasons. First, the peak energy is well-above the bandgap

of pentacene so that both absorption and photocurrent yield are negligible at this energy and the widely accepted mechanism of Figure 4.2a can not be applied. Second, even though signal is detected from many charges in different microstructural and electrostatic environments, a comparatively narrow and well-defined trap-clearing action spectrum is observed.

To account for these experimental observations, an alternative trap-clearing mechanism is proposed. In Figure 4.2c, trap clearing by another kind of photoinitiated electron transfer is shown. In step 4 of the figure, a positively charged chemical impurity is optically excited. The optical excitation does not necessarily have to be the lowest energy excitation. The trap is cleared in step 5 via backfilling through an electron transfer from a nearby pentacene molecule and the resulting hole is transported away (step 6).

A state diagram summarizing the two mechanisms is shown in Figure 4.2d. This figure highlights that the neutral, open-shell $T^{\bullet}$ species resulting from both trap-clearing mechanisms may undergo further chemical reactions to yield a neutral, closed-shell trap precursor. This observation supports conjecture of Lang et al. that atomic motion plays a key role in the quenching of charge traps. [41]

To explain the observed trap-clearing action spectrum by the mechanism of Figure 4.2c, an impurity or defect in the pentacene solid must be present that exhibits an optical excitation near 500 nm. Time-dependent density-functional theory (TDDFT) was used to calculate the optical spectra for two defects proposed as hole traps [57] (shown in Figure 4.3) as well as for pentacene. These two charged defects are the expected products of the reaction of pentacene cation radicals (e.g., holes) with the neutral trap precursors 6,13-dihydropentacene and pentacen-6(13H)-one impurities, respectively.

4.2 Computational Details

density-functional theory (DFT) and time dependent density-functional theory (TDDFT) calculations were performed using Gaussian 09 [21, 8] with the B3LYP [9] functional and the 6-311++G(d,p) basis. The appendix contains an example input file, and the subtleties involved in the software, functional, and basis are detailed below.

Gaussian, the computational software package, uses sums of gaussian functions localized around each atom in a molecule to expand the wavefunctions of the molecules. This is in contrast to the plane-wave expansions preferred in solid-state computational software packages. Because the calculations performed involve a single molecule, the Gaussian package was chosen.

The B3LYP functional is known as a hybrid exchange-correlation functional. It contains a linear combination of exact exchange (from Hartree-Fock theory), and density-functional correlation components from the local density approximation and the generalized gradient approximation. The coefficients for the linear combination were determined empirically by Becke, Lee, Yang, and Parr (the ”B” and ”LYP” in B3LYP) [9]. It is important to note that different versions of B3LYP have been published and implemented, and the version implemented in Gaussian differs from that used in, for example, the software package Gamess. The minor differences in parameter choice creates small differences in the energies of these molecules, so that absolute energies between codes may not agree.

The 6-311++G(d,p) basis is known as a Pople basis set, and it was designed by the John Pople group. The Pople basis sets have been well-studied for use in density-functional theory calculations, although there are other suitable basis set choices. The nomenclature of the basis identifies the number and types of functions included in the

basis. Each carbon and hydrogen in the pentacene molecule wavefunction in the 6-311++G(d,p) basis contain six Gaussians used to describe the atomic orbital's core, and the valence orbitals are described by linear combinations of one function containing three Gaussians, and two functions each with one Gaussian. The plus signs indicate that additional diffuse Gaussians were included in the basis. These extra Gaussians are particularly important for the description of excited states that are expected to be less localized than the ground state of the system. The excited state must be described equally as well as the ground state, because the quantity of interest is energy differences between the two states. If the basis is not sufficiently flexible to describe the excited state wavefunction, then the energy associated with that state, and hence the energy difference, will be overestimated.

The basis set was converged using the frequency of pentacene's first singlet excited state, the main peak in Figure 4.1. Changes in this value were less than 4 nm (0.01 eV) for the 6-311++G(d,p) compared to the 6-311+G(d) basis. Individual properties such as the frequency of a given excited state converge differently with basis set size — some properties are better described when diffuse functions are added, and others improve more significantly with additional polarization functions. For this reason, I study convergence as a function of the frequency of an excited state similar to the states that I hope to investigate.

Defect molecule geometries and ground state energies were found by optimizing single-defect molecule geometries with the 6-311++G(d,p) basis and B3LYP. To approximate the chemical environment of the pentacene molecular solid, DFT and TDDFT calculations were performed with solvation in a dielectric medium using the polarizable continuum model (PCM) [53] with a dielectric constant of 4.82, as suggested by previous calculations. [54] Dielectric constants from 3 to 6 were examined and the calculated

first singlet excitation frequency in pentacene was found to vary by no more than a few nanometers.

4.3 TDDFT Calculations

Time-dependent density-functional theory (TDDFT) was used to calculate the optical spectra for two defects proposed as hole traps [57] (shown in Figure 4.3) as well as for pentacene. These two charged defects are the expected products of the reaction of pentacene cation radicals (e.g., holes) with the neutral trap precursors 6,13-dihydropentacene and pentacen-6(13H)-one impurities, respectively. [57] In the calculations a dielectric continuum model was used to describe the surrounding pentacene molecules. While TDDFT is less accurate for certain excitations in gas-phase acene molecules [23, 35], using TDDFT to calculate the energies of a molecule embedded in a dielectric continuum has been shown to accurately describe most excitations in the bulk acenes [54]. Of course, the use of a dielectric model in place of explicit pentacene molecules will mean that only inter-molecular excitons are considered, and excitons spanning multiple molecules will not be considered. More accurate calculations, such as full crystalline calculations including surrounding pentacene molecules, or the GW approximation for the BetheSalpeter equation (GW-BSE) [84], are computationally very expensive for defect calculations and beyond the scope of this project.

However, others have used higher methods to examine the excited states of pentacene. The singlet excitations of the oligoacenes are well-studied, and great interest currently surrounds the excited singlet states of pentacene. These states have been shown to convert into two triplet excitations, through a process known as singlet fission, whose mechanism is still debated [10, 96, 76]. (This process potentially can be

used to increase the efficiency of solar cells, as photons with energy well above the bandgap of pentacene can be used to generate two excitons that can be used for energy, rather than being wasted as heat [76].) The singlet states can be divided into two types — those referred to as "p-band" type, where the excitation polarizes the short axis of the oligoacene, and "α and β" types, where the excitation is polarized along the long axis [35]. The α and β type excitations are well-predicted in TDDFT, whereas TDDFT calculations of the p-type excitation do not match well with other quantum chemistry calculations or experiment [35]. A better understanding of this failure is an area of active research [26].

4.4 Results

The solid black lines in Figure 4.3 show the TDDFT spectra computed using a Gaussian broadening and the TDDFT oscillator strengths for the amplitudes. As seen in Figure 4.3a, the calculation correctly predicts the peak at 675 nm in the pentacene absorption spectrum. Figure 4.3b shows that the oxygen defect has a predicted absorption near λ = 500 nm while the hydrogen defect does not. This finding indicates that the oxygen defect and not the hydrogen defect is the source of the unexpected above bandgap peak observed in the trap-clearing spectra of Figure 4.1c,d. The lack of a similarly intense trap-clearing peak at 630 nm can be rationalized in terms of the mechanism of Figure 4.2c by considering that trap clearing depends on intermolecular electron transfer as well as on absorption.

j	λ_j [nm]	f_j
1	676.6	0.0753
2	422.7	<0.0001
3	394.3	<0.0001

Table 4.1: Singlet excitations of pentacene calculated using TDDFT as discussed in the text. The calculated wavelength λ and oscillator strength f are listed for the three lowest optical excitations j.

	Trap species 1		Trap species 2	
j	λ_j [nm]	f_j	λ_j [nm]	f_j
1	643	0.02	630	0.72
2	587	0.55	561	0.02
3	451	1.05	526	0.00
4	343	0.02	508	0.55
5	317	0.01	367	0.11

Table 4.2: Singlet excitations calculated using TDDFT for defects 1 and 2 shown in Figure 4.4 and Figure 4.5, respectively. The calculated wavelength λ and oscillator strength f for the five lowest optical excitations j is shown

4.5 Discussion: Trapping Mechanisms And Precursers

In Figure 4.3b, the spectra of two cationic trap species were presented. Here I detail possible mechanisms for forming these species from precursors. The oxygen-containing impurity species in Figure 4.3b was hypothesized by Northrup and Chabinyc [78] to form by the chemical reaction of a 6,13-dihydropentacene impurity with two pentacene cation radicals (e.g., holes). Two proposed mechanisms for this reaction are presented in Figure 4.4.

Both mechanisms begin with a hydrogen transfer. The first mechanism proceeds to the trap species via an electron transfer. The second mechanism proceeds to the trap species via a hydrogen atom transfer reaction. Note that both mechanisms result in the same cationic impurity species (the molecules boxed in red in the figure). I hypothesize

Excitation 1 (630 nm)			Excitation 2 (508 nm)		
initial	final	coeff.	initial	final	coeff.
HOMO-2	LUMO	-0.14	HOMO-2	LUMO	+0.69
HOMO	LUMO	+0.69	HOMO	LUMO	+0.14

Table 4.3: Conguration-interaction expansion coefficients for the two dominant excitations of defect 2.

that the second impurity species in Figure 4.3 forms by a reaction of pentacen-6(13H)-one with two pentacene cation radicals. A proposed mechanism for this reaction is shown in Figure 4.5. Note that the mechanism leads to the formation of both the hydrogen and oxygen impurities. The energies of these two trap-forming reactions are given in the captions of Figure 4.4 and Figure 4.5. The reaction free energies depend also on the concentration of available free holes (e.g., the electron chemical potential or Fermi level), as described by Northrup and Chabinyc [78].

While the reaction in Figure 4.4 is slightly more energetically favorable than the reaction of Figure 4.5, I predict that the activation barrier of the rate determining step in Figure 4.5 is slightly lower than for the rate determining step in Figure 4.4. The first step of both of these reactions, the hydrogen transfer, appears to be stabilized by the presence of the (dipole moment of the) oxygen, as shown by the resulting lower energy of the first step in Figure 4.5. Following the Hammond-Leffler Postulate, I expect a smaller activation barrier to the hydrogen transfer reaction in Figure 4.5. If the first step is rate limiting, and the amount of defect is governed by kinetics and not thermodynamics, then this difference in activation energies might explain why we see primarily the oxygen-defect cation the trap-clearing spectra of Figures 4.1 and 4.3.

To clear the trap, an electron must be transferred from a neighboring pentacene molecule into the state vacated by the photoexcited electron before the optically excited electron relaxes back to its initial state. To regenerate the trap precursor (either 6,13-

dihydropentacene or pentacen-6(13H)- one) requires the transfer of a proton as well. The rate of electron transfer, proton transfer, and non-radiative decay can be calculated in principle, but these calculations are beyond the scope of this project.

Density-functional theory (DFT) and time dependent density-functional theory (TDDFT) calculations were performed as previously described in the Computational Details section. For the bulk phase acenes, we investigated the lowest singlet excitations, comparing TDDFT results [57] to experimental findings. [50, 41] As shown in Table 4.5, the experimental and TDDFT results agree well. The calculated singlet transitions in Table 4.5 were used to compute the pentacene absorption spectrum (the solid black line in Figure 4.3a) via the formula

$$\mathrm{Abs}(\lambda) = c \sum_{j=1}^{3} f_j \exp\left(\frac{-(\lambda - \lambda_j)^2}{2\Delta\lambda^2}\right), \tag{4.1}$$

where the normalization constant c and linewidth $\Delta\lambda$ =15nm were varied by hand to maximize agreement between the calculated and observed absorption spectrum. Looking at Figure 4.3a, the dielectric continuum solvation model employed here correctly predicts the energy of the low-energy Frenkel exciton - localized over a single molecule - at 675 nm in the experimental pentacene absorption spectrum [41]. The peak in the experimental spectrum at 575 nm corresponds to an intermolecular charge transfer exciton [39] and the peak near 630 nm arises from the Davydov crystal-field splitting [41]. To predict the energies of these peaks, one must move beyond a solvation model and explicitly include the neighboring pentacene molecules. Since these types of excitations are not expected to be involved in the observed trap clearing at 500 nm, I do not consider them here.

The results of TDDFT calculations carried out for defects 1 and 2 are presented in Table 4.5. The calculated singlet transitions in Table 4.5 were used to compute the trap clearing spectra using formulas analogous to Equation 4.1, with $\Delta\lambda$ =28 nm. The

calculated spectra are shown as solid black lines in Figure 4.3b. The oxygen defect 2 has a predicted absorption feature near λ = 500 nm while hydrogen defect 1 does not, indicating that the oxygen defect and not the hydrogen defect is the source of the unexpected peak in the observed trap-clearing spectrum of Figure 4.1c,d. The TDDFT calculation also predicts a λ = 630 nm peak in defect 2's absorption spectrum which is not apparent in the observed trap-clearing spectrum. We must also take into account, however, that the rate of charge-trap clearing at a given wavelength will also depend on the probability of inter- and intra-molecular electron transfer reactions, as indicated in Figure 4.2a-c. Consider, for example, the mechanism shown in Figure 4.2c. To clear the trap, an electron must be transferred from a neighboring pentacene molecule into the state vacated by the photoexcited electron before the optically excited electron relaxes back to its initial state. Furthermore, in both the mechanisms sketched in Figure 4.2, to regenerate the trap precursor either 6,13-dihydropentacene or pentacen-6(13H)-one requires the transfer of a proton as well.

The rate of electron transfer, proton transfer, and non-radiative decay can be calculated in principle, but these calculations are beyond the scope of this project. Nevertheless, our TDDFT results can be used to rationalize why defect 2's λ = 508 nm transition might contribute more to the trap-clearing spectrum that its λ = 630 nm transition. In Table 4.5, I show the configuration-interaction expansion coefficients for the two dominant excitations of defect 2. The first excitation of defect 2, at 630 nm, is predominantly a HOMO $\rightarrow$ LUMO transition, whereas the fourth excitation, at 508 nm, is dominated by a HOMO-2 $\rightarrow$ LUMO transition. The relevant orbitals are plotted in Figure 4.6. The HOMO-2 is strongly localized on the oxygen atom while the HOMO is delocalized over the whole defect molecule. Because of this localization, we would expect the HOMO-2 orbital to have greater orbital overlap than would the LUMO orbital with the highest occupied molecular orbital of pentacene. Additionally, the polarization of the excited

state is expected to be greater for the fourth singlet excitation. Both of these factors predict that the electron-transfer rate should be larger for the 508 nm excitation of defect 2 than for the 630 nm excitation, in qualitative agreement with what is observed in the trap-clearing spectrum.

4.6 Discussion: Other Possible Defects

Until this point, only two possible chemical trap species have been considered. This work does not eliminate the possibility of a yet unexplored trap species that is responsible for the absorption profile seen in experimental work. Here, other possible traps are considered.

Gap states can potentially form as a consequence of the dipole of a polar defect molecule, stabilizing the hole state of pentacene. The defect molecule's composition is perhaps of less importance than the presence and strength of its dipole moment. The formation of these gap states was examined for the species previously assumed to be the oxygen-defect precursor, for water, and for pentaquinone.

The oxygen defect previously assumed to be the oxygen-defect precursor can bend along the long axis of the pentacene backbone and form a gap state predicted by preliminary B3LYP calculations[2] at around 0.43 eV. This deformation is demonstrated in Figure 4.7. The formation of this charged defect (versus a neutral oxygen defect precursor and a pentacene hole) is favored in a B3LYP calculation by 0.398 eV. If the reaction barrier to structural deformation is not too large, this reaction could potentially explain the experimental results in an alternate way. The frequency of light needed to clear this

[2]These calculations were performed with the relatively small 6-31G basis set, because the number of atoms per calculation is approximately twice as large as needed for the other calculations investigated for this thesis.

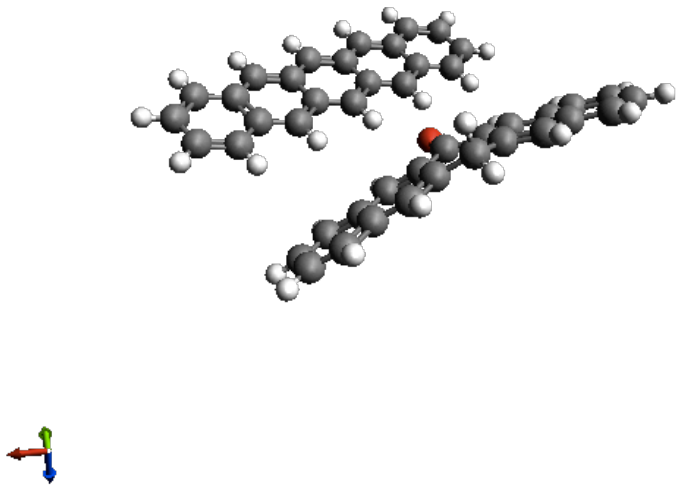

Figure 4.7: The pentacene hole and adjacent oxygen defect, bent towards the hole.

trap is currently unknown, however, given that the TDDFT calculation would require two molecules, and this was too computationally expensive to perform for this thesis.

Water and pentaquinone were also considered as potential trap species, but both had shallower gap states than the oxygen defect, although the pentaquinone defect was in the correct range. The oxygen defect in particular seems to have a stabilizing effect on the pentacene, and should be considered still as a possible trap species.

4.7 Conclusion

In summary, *ab initio* theory was used to elucidate mechanisms of light-induced trap clearing in polycrystalline pentacene. Previously proposed mechanisms of trapping and

detrapping involving midgap states at intragrain regions [68, 49], the formation of immobile bipolarons [78], molecular sliding [36], the migration of charge into dielectric layers [49], the stabilization of charges by dipoles in dielectric layers [89, 40], or chemical reactions in the bulk [57, 39]. But these mechanisms cannot simultaneously explain the spatial distribution of traps and the wavelength dependence of trap clearing observed here. A new mechanism of trap clearing via photoexcitation of the trap species followed by electron transfer was suggested; the spectroscopic trap-clearing data implicate pentacen-6(13H)-one as the relevant neutral trap precursor.

4.8 Acknowledgements

Justin Luria co-wrote the manuscript, and collected and analyzed experimental data. Michael Jaquith and Justin Luria significantly modified custom microscopes for experimental data collection. Richard Hennig oversaw the theory portion of the project. John Marohn oversaw the project, analyzed data, and co-wrote the manuscript. Funding was provided by the NSF (DMR-0706508, ECS-0335765, EAR-0703226, and a Graduate Research Fellowship) and the DOE (DE-FG05-08OR23339). Computational resources were provided by NCSA,NERSC, and CCNI.

CHAPTER 5

DIELECTRIC APPROXIMATIONS OF THE DIELECTRIC MATRIX IN MOLECULAR CRYSTALS

5.1 Introduction

Recent advances in organic electronics have spurred interest in molecular solids and liquids for dielectric and optical applications [19, 73, 52]. The behaviors of these materials are typically assessed through experiments, although the performance of these materials can be altered by uncharacterized structural defects and impurities [48]. A computational approach to better understand and predict the dielectric and optical properties of these materials would complement experimental work, facilitating further advances in the characterization and design of new materials.

Current state-of-the-art solid state dielectric calculations are limited to systems smaller than a typical molecular crystal of interest in organic electronics, or the calculations rely on simplifications (See for instance Ref. [29]). Quantum chemistry calculations also have molecule size limitations, and additionally have basis convergence complications. They also do not have a systematic way to deal with the environment surrounding the molecule. Additionally, current computational approaches do not leverage the repeated molecular structure of molecular crystals and liquids, requiring independent calculations for molecules in crystal polymorphs, and in different molecular configurations in a liquid.

The repeated, periodic structure of a molecular crystal presents an opportunity that has yet to be exploited. Here, we describe a method to calculate the optical dielectric response of molecular crystals and liquids that takes advantage of the modularity of these

systems. This method allows for the calculation of large molecular crystals and liquid configurations — at less cost than an equivalently converged solid-state calculation. Below, we detail the general theory of our approach, followed by the implementation of the method, and then we discuss results for hexagonal ice and solid benzene applications.

5.2 General Theory

The full inverse microscopic dielectric matrix $\epsilon^{-1}(r, r')$, the central quantity in describing the dielectric response of a system, expresses the linear response ϕ_{tot} of the *total* electrostatic potential to the application of an *external* potential ϕ_{ext} through

$$\phi_{tot}(r) = \int d^3r' \, \epsilon^{-1}(r, r')\phi_{ext}(r'). \tag{5.1}$$

In the below, we find it convenient to employ a representation-independent, operator-based notation, so that (5.1) appears as $\phi_{tot} = \epsilon^{-1}\phi_{ext}$. Continuing with this notation, we note that the operator most directly accessible to microscopic calculations is the *external* susceptibility χ_{ext}, which gives the first-order induced change in the charge density ρ_{ind} through the linear-response relation $\rho_{ind} = \chi_{ext}\,\phi_{ext}$. Given this response function, one can then compute the corresponding *induced* potential through $\phi_{ind} = K\rho_{ind}$, where the Coulomb operator $K(r, r') \equiv 1/|r - r'|$ in the standard atomic units in which we work. It is also useful to define a *total* susceptibility χ_{tot}, linking the linear response in the charge density to the *total* response potential, $\rho_{ind} = \chi_{tot}\,\phi_{tot}$. Finally, direct substitution of these relations into the decomposition of the total response potential, $\phi_{tot} = \phi_{ind} + \phi_{ext}$ then gives the standard connections between the microscopic dielectric response and susceptibility functions,

$$\epsilon^{-1} = 1 + K\chi_{ext} \tag{5.2}$$

$$\epsilon = 1 - K\chi_{tot}, \tag{5.3}$$

from which also follows a Dyson relation for χ_{ext} in terms of χ_{tot},

$$\chi_{ext} = \chi_{tot} + \chi_{ext} K \chi_{tot}. \tag{5.4}$$

At this stage, no approximations have been made, and χ_{ext} can be extracted, in principle, directly from correlated electronic structure methods, such as coupled-cluster (CC) or quantum Monte Carlo (QMC) [87], by observing the response of the system under consideration to the application of a (large) set of perturbing external potentials. However, this approach becomes prohibitive for all but the smallest systems.

Electronic band-structure approaches, while much more practical, unfortunately do not give direct access to χ_{ext} or χ_{tot}, but rather to χ_{ni}, the (zero frequency) response of a *non-interacting* system of orbitals to changes in their *external* potential, which has the explicit form

$$\chi_{ni}(r, r') = \sum_{i \neq j} \frac{f_i - f_j}{\epsilon_j - \epsilon_i} [\psi_i^*(r)\psi_j(r)\psi_j^*(r')\psi_i(r')], \tag{5.5}$$

where f_i and ϵ_i are the filling factor (ranging from zero to one) and eigenvalue of the ith band, respectively. The Kohn-Sham theorem ensures that the density-response of such a non-interacting system to changes δV_{KS} in the self-consistent *Kohn-Sham* potential gives the *exact* density-response of the fully interacting system, so that, *exactly*, $\rho_{ind} = \chi_{ni}\, \delta V_{KS}$. The first-order response of the Kohn-Sham potential includes responses in the external, Hartree, and exchange-correlation components, respectively, $\delta V_{KS} = \phi_{ext} + K\rho_{ind} + C\rho_{ind} = \phi_{tot} + C\rho_{ind}$, where K is the Coulomb operator defined above, and $C(r, r') \equiv \delta^2 E_{xc}/(\delta\rho(r)\, \delta\rho(r'))$ gives the response of the exchange-correlation potential to changes in the electron density. Combining these preceding two forms for δV_{KS} with $\rho_{ind} = \chi_{ext}\phi_{ext}$ and $\rho_{ind} = \chi_{tot}\phi_{tot}$, respectively, yields the following two *exact* Dyson relations for the microscopic susceptibilities,

$$\chi_{ext} = \chi_{ni} + \chi_{ni}(K + C)\chi_{ext} \tag{5.6}$$

$$\chi_{tot} = \chi_{ni} + \chi_{ni} C \chi_{tot}, \tag{5.7}$$

which may then be combined with (5.2,5.3) to yield the microscopic dielectric response.

Even with the relative economy of band-structure based methods, the standard approach of going from (5.5) through (5.6,5.7) and finally to (5.2,5.3) is limited to relatively simple systems due to the need to compute a prohibitive number of empty bands to converge the sum in (5.5). While a number of interesting approaches for decreasing these costs have been proposed [12, 86, 66], these approaches would still require separate electronic band-structure calculations for each configuration of a liquid, or for each defect studied in a molecular crystal. A more efficient method for the dielectric response of solvated or molecular crystalline systems would thereby open a new range of problems for first principle studies.

5.2.1 *Molecular Separation* Ansatz

The first key observation of this work is that, to a good approximation, for closed-shell molecular systems both χ_{ni} and χ_{tot} can be well-approximated as sums of independent localized molecular contributions, resulting in a radical simplification of the calculations necessary to determine the dielectric properties of a molecular crystal or liquid. This decomposition also provides, for the first time, a practicable method for including high-order electron-correlation effects into the dielectric response of large collections of molecules.

The efficacy of the decomposition of χ_{ni} into a sum

$$\chi_{ni}(r, r') = \sum_R \chi_{ni}^{[m]}(r - R, r' - R) \tag{5.8}$$

of individual *molecular* density-response functions $\chi^{[m]}(r, r')$ stems directly from the structure of (5.5) for closed-shell molecular systems. For such systems, the relative electronic isolation of the molecules ensures little dispersion in the eigenvalues ϵ_i, allowing

for unitary transformation among the bands to maximally localized orbitals, without affecting the value of either the i or j sums in (5.5). Moreover, under these conditions, the maximally localized orbitals will closely resemble the molecular orbitals so that, to a good approximation, the i and j sums can be taken to range over the molecular orbitals of the system. Finally, the relative lack of overlap between orbitals on *different* molecules ensures that both factors $\psi_i^*(r)\psi_j(r)$ and $\psi_j^*(r')\psi_i(r')$ in the numerator of (5.5) will be small and, therefore, that only terms with i and j on the same molecule contribute significantly to the final result. Keeping only these terms and replacing the orbitals and eigenvalues with the corresponding molecular quantities then leads directly to (5.8).

The observation that χ_{tot} may likewise be decomposed, $\chi_{tot}(r, r') = \sum_R \chi_{tot}^{[m]}(r-R, r'-R)$ follows from Dyson iteration of (5.7). Because the major contributions to E_{xc} are reasonably well-approximated by local- or semilocal- density functionals, we expect that $C(r, r')$ only weakly connects points r and r' residing on different molecules. This, combined with the above anticipated decomposition of $\chi_{ni}^{[m]}$ into localized molecular contributions, ensures that iteration of (5.7) does not generate strong inter-molecular connections in χ_{tot}, so that a molecular decomposition of χ_{tot} analogous to (5.8) should also yield a good approximation. Ultimately, the suitability such of molecular decompositions of χ_{ni} and χ_{tot} can only be evaluated through calculations of realistic systems, as we perform below.

5.3 Implementation

The second key observation in this work is that the collection of the eigenfunctions of the *non-interacting* response function $\chi_{ni}^{[m]}$ from *each individual molecule m* in the system provides a well-converging, albeit non-orthogonal, basis for dielectric response

calculations. We explored also use of the eigenstates of $\chi_{tot}^{[m]}$, but found the eigenstates of $\chi_{ni}^{[m]}$ to present the fewest numerical problems. Although similar susceptibility eigenbasis approaches have been pursued in the past [47, 92, 91], this work is the first to exploit the significant computational advantages of the decomposition into individual molecular response functions. Here, we represent the eigendecomposition of the noninteracting molecular susceptibility of each molecule m as

$$\chi_{ni}^{[m]} = V^{[m]} X_{ni}^{[m]} V^{[m]\dagger}, \tag{5.9}$$

where $X_{ni}^{[m]}$ is a diagonal matrix containing the eigenvalues and $V^{[m]}$ is a matrix containing the eigenfunctions, arranged so that the nth column of $V^{[m]}$ contains a convenient computational representation of the nth eigenfunction, such as real-space samples or a plane-wave expansion. Finally, in this expression, the † operator implements the integral overlap between eigenfunctions so that $V^{[m]\dagger} V^{[m]} = I$. If, for example, a representation of real-space samples is chosen, then † will include a factor of the volume associated with each sample point so that properly normalized numerical integrations are carried out.

Dyson iteration of (5.6,5.7) then establishes that both the external and total molecular susceptibilities take the form (5.9), with matrix elements $X_{ext}^{[m]}$ and $X_{tot}^{[m]}$, respectively, obeying

$$X_{ext}^{[m]} = X_{ni}^{[m]} + X_{ni}^{[m]} (\bar{K}^{[m]} + \bar{C}^{[m]}) X_{ext}^{[m]} \tag{5.10}$$

$$X_{tot}^{[m]} = X_{ni}^{[m]} + X_{ni}^{[m]} (\bar{C}^{[m]}) X_{tot}^{[m]}, \tag{5.11}$$

where $\bar{K}^{[m]} \equiv V^{[m]\dagger} K V^{[m]}$ and $\bar{C}^{[m]} \equiv V^{[m]\dagger} C V^{[m]}$ are the matrix elements of the corresponding operators in the $V^{[m]}$ basis. Below we will demonstrate that the number of eigenvectors required is on the order of several hundred per molecule (and generally much smaller than the number of filled-empty pairs ij needed to converge the sum (5.5)), so that the preceding relations are readily handled on even modest workstations.

To work within a density-functional theory framework, the matrix elements $X_{ext}^{[m]}$ or $X_{tot}^{[m]}$ are readily obtained by solving (5.10,5.11), yielding for example the easily computed expression $X_{tot}^{[m]} = (1 - X_{ni}^{[m]}\bar{C}^{[m]})^{-1}X_{ni}^{[m]}$. In the case of a fully correlated method, one would compute $X_{ext}^{[m]} = V^{[m]\dagger}(\chi_{ext}V^{[m]})$ by first applying each column of $V^{[m]}$ as an external potential ϕ_{ext} to the correlated molecular calculation , then extracting the (first-order) induced charge response ρ_{ind} by finite differencing or a linear response method, and finally computing the overlaps $V^{[m]\dagger}\rho_{ind}$. With $X_{ext}^{[m]}$ in hand, one may then employ (5.4) to determine the total fully correlated molecular response function through $X_{tot}^{[m]} = (1 + X_{ext}^{[m]}\bar{K}^{[m]})^{-1}X_{ext}^{[m]}$. In this way, several hundred correlated electronic structure calculations on a *single* molecule can be used to build up the fully correlated dielectric response function for large collections of molecules.

Crystalline systems The treatment of periodic systems is best accomplished through transformation to a Bloch-periodic basis,

$$V(k) = \sum_m e^{ik\cdot R_m}V^{[m]}, \tag{5.12}$$

where k is the Bloch character of the particular basis formed, $V^{[m]}$ are the eigenfunctions for molecule m, R_m is the location of molecule m, and we take the R_m to form a periodic lattice. (For crystals with primitive cells containing multiple molecules, we formally consider the primitive cell as a "meta-molecule", with the states of each separate molecule represented as a block of columns in $V^{[m]}$ and the corresponding matrix elements appearing in diagonal blocks in $X_{ext}^{[m]}$ and $X_{tot}^{[m]}$.) One then obtains the standard result that, *for functions of Bloch character k*, the action of a full crystal operator of the additive form (5.8) is equivalent to that of the operator

$$\chi(k) \equiv V(k)X^{[m]}V(k)^\dagger, \tag{5.13}$$

where the inner product associated with † now represents integration over the unit cell of the crystal lattice, rather than the entire space. Finally, note that here and below,

quantities referring to the entire crystal will carry a k dependence, whereas quantities referring to a single molecule with carry the superscript $[m]$. Given that χ_{ni} is of the form 5.13, Dyson iteration of (5.7,5.6) leads to conclusions directly analogous to those leading up to (5.10,5.11) above, namely that the operators $\chi_{ext}(k)$ and $\chi_{tot}(k)$ are also of the form (5.13, but with k-dependent matrix elements obeying,

$$X_{ext}(k) = X_{ni}^{[m]} + X_{ni}^{[m]}\left(\bar{K}(k) + \bar{C}(k)\right)X_{ext}(k) \tag{5.14}$$

$$X_{tot}(k) = X_{ni}^{[m]} + X_{ni}^{[m]}\bar{C}(k)X_{tot}(k), \tag{5.15}$$

with $\bar{C}(k) \equiv V(k)^{\dagger}CV(k)$ and $\bar{K}(k) \equiv V(k)^{\dagger}KV(k)$. And, analogously to (5.4), we find

$$X_{ext}(k) = X_{tot}(k) + X_{ext}(k)\bar{K}(k)X_{tot}(k). \tag{5.16}$$

When working with density-functional based methods, the matrices $X_{ni}^{[m]}$ come directly from the molecular calculations and are thus k-independent and require no special calculation. The matrix elements $\bar{C}(k)$ are best computed directly in real space due to the (semi-)local nature of common exchange-correlation functionals. Moreover, the relative lack of overlap between eigenstates from different molecules m and m' provides confirmation of our observations regarding χ_{tot} above. Specifically, this lack of overlap implies that, to a good approximation, one may take $\bar{C}(k)$ as consisting of diagonal blocks of the corresponding the molecular values, $\bar{C}(k) \approx \bar{C}^{[m]}$. Through (5.15) this approximation would yield a k-independent $X_{tot}(k)$ consistent with our observations above that χ_{tot} should be similarly amenable to additive decomposition of the form (5.8).

Finally, the matrix elements $\bar{K}(k) = V(k)^{\dagger}KV(k)$ are best computed in reciprocal space due to the extended nature of the Bloch basis functions. To evaluate these, we note that the standard Wannier transformation (5.12) gives the real-space representation of the nth column of $V(k)$ as

$$V_{nk}(r) = \frac{1}{\Omega}\sum_{G}\hat{V}_{G,n}(k)e^{i(k+G)\cdot r}, \tag{5.17}$$

where Ω is the volume of the crystal unit cell, and the matrix elements $\hat{V}_{G,n}(k) \equiv \hat{V}_n(k+G)$ are defined directly from the Fourier components $\hat{V}_n(q) = \int d^3r\, e^{-iq\cdot r} V_n(r)$. Then, employing the fact that the action of the Coulomb operator in reciprocal-space is multiplication by a diagonal matrix with elements $\hat{K}(k) = 4\pi/|k+G|^2$ and noting that the range of integration represented by † is a single unit cell, we have $\bar{K}(k) = \left(\hat{V}(k)^\dagger \hat{K}(k) \hat{V}(k)\right)/\Omega$.

For working with correlated methods, we would recommend substituting the molecular matrix elements $X_{tot}^{[m]}$, obtained as described above, into the Bloch form for additive operators (5.13) yielding $\chi_{tot}(k)$. Then, to obtain $\chi_{ext}(k)$ one would employ the crystal Dyson equation (5.16), obtaining the matrix elements

$$X_{ext}(k) = X_{tot}(k)\left(1 - \bar{K}(k) X_{tot}(k)\right)^{-1}. \tag{5.18}$$

Finally, armed with the matrix elements and Bloch representations (5.13) for $\chi_{ext}(k)$ and $\chi_{tot}(k)$, one may employ (5.2) and (5.3), respectively, to build the full crystal dielectric response operators, yielding in the former case

$$\epsilon^{-1}(k) = 1 + KV(k) X_{ext}(k) V(k)^\dagger. \tag{5.19}$$

To determine, for example, the spectrum of $\epsilon^{-1}(k)$, as we do below, one notes that eigenvectors must come in the form of linear combinations of the columns of $KV(k)$, so that one need only find the right eigenvalues of the matrix $1 + [V(k)^\dagger KV(k)]X_{ext} \equiv 1 + \bar{K}(k) X_{ext}(k)$, a matrix of manageable size that is explicitly computable from the results above.

5.4 Macroscopic equations

Determination of the *macroscopic* equations and dielectric tensor $\bar{\epsilon}$ requires connecting the *scalar* microscopic response theory to the macroscopic *vector* equations. This con-

nection is most clear in Fourier space, where the Poisson equations for the *macroscopic* total potential $\bar{\phi}_{tot}$ and *macroscopic* external potential $\bar{\phi}_{ext}$ appear as $k^\dagger \bar{\epsilon} k \bar{\phi}_{tot} = 4\pi\rho_{ext}$ and $|k|^2\bar{\phi}_{ext} = 4\pi\rho_{ext}$, respectively, where k is the wave *vector* associated with the macroscopic perturbation. (Note that because the $|k| \to 0$ limit required below involves critical distinctions between direction and magnitude, we shall henceforth employ the explicit notation $|k|$ when referring to the *magnitude* of k.) Equating the preceding relations yields $\hat{k}^\dagger \bar{\epsilon} \hat{k} = \bar{\phi}_{ext}/\bar{\phi}_{tot}$. Thus, the anomalous, directional dependence of the $k \to 0$ limit of the microscopic dielectric response *reflects directly* the *tensor* nature of the macroscopic dielectric constant.

The *macroscopic* fields in the above paragraph represent smooth functions, averaged over the unit cells of the crystal and thus exhibit only long-wavelength behavior. A suitable choice for the (applied) external potential is thus $\bar{\phi}_{ext} = \phi_0 e^{ik\cdot r}$, or equivalently $\phi_{ext,G}(k) = \phi_0 \delta_{G,0}$ where δ is the Kronecker delta function. The microscopic response of the material system to this applied potential, $\phi_{tot} = \sum_G \phi_{tot,G}(k) e^{i(k+G)\cdot r}$, will include short wave-length $G \neq 0$ components which average to zero over the unit cell, so that $\bar{\phi}_{tot} = \phi_{tot,G=0}(k) e^{ik\cdot r}$, and the right side of (5.20) becomes $\phi_0/\phi_{tot,G=0}(k) = \left(\epsilon^{-1}_{0,0}(k)\right)^{-1}$, where the last term is the inverse of the $(G, G') = (0, 0)$ matrix element of the inverse microscopic dielectric response operator for functions of Bloch character $\mathbf{k}$. We thus conclude that, in the macroscopic limit,

$$\hat{k}^\dagger \bar{\epsilon} \hat{k} = \left(\lim_{|k|\to 0} \epsilon^{-1}_{0,0}(k) \right)^{-1}. \tag{5.20}$$

To evaluate (5.20), note that (5.19) gives

$$\epsilon^{-1}_{0,0}(k) = 1 + \frac{1}{\Omega} \frac{4\pi}{k^2} \hat{V}_0(k) X_{ext}(k) \hat{V}_0^\dagger(k), \tag{5.21}$$

where, from the Fourier transform convention defined above, the asymptotic behavior

of the components of the row vectors $\hat{V}_0(k)$ is

$$\hat{V}_0(k) \xrightarrow{k\to 0} -ik^\dagger P + O(k^2), \tag{5.22}$$

with

$$P_{\alpha,n} \equiv \int d^3r\, V_n(r) r_\alpha \tag{5.23}$$

being the elements of a matrix, each of whose columns contains the Cartesian coordinates of the dipole moment of a given eigenfunction V_n. The limit of (5.21) is thus

$$\epsilon^{-1}_{0,0}(k) \xrightarrow{k\to 0} 1 + \frac{4\pi}{\Omega}\hat{k}^\dagger P X_{ext}(k) P^\dagger \hat{k} + O(k). \tag{5.24}$$

The external susceptibility matrix elements $X_{ext}(k)$ themselves also exhibit anomalous k-direction behavior, due to the presence in (5.18) of $\bar{K}(k)$, which exhibits irregular $k \to 0$ behavior due to the singular nature of the $G = 0$ component of the diagonal operator $\hat{K}(k) = 4\pi/|k+G|^2$. Separating out the singular $G = 0$ term gives

$$\bar{K}(k) \xrightarrow{k\to 0} \bar{K}_H + \frac{4\pi}{\Omega} P^\dagger \hat{k}\hat{k}^\dagger P, \tag{5.25}$$

where $\bar{K}_H \equiv [\hat{V}(0)^\dagger K(k=0)\hat{V}(0)]_{G\neq 0}$ is the $k = 0$ Coulomb sum for electrostatic interactions among the columns of $\hat{V}$ *but with the* $G = 0$ *term omitted*, namely what typical plane-wave implementations compute as the "Hartree" interaction. Combining (5.18,5.25) then gives the small k behavior of $X_{ext}(k)$ through a two-step renormalization process

$$\begin{aligned} \bar{X}_{ext} &\xrightarrow{k\to 0} X_{tot}(k=0)\left(1 - \bar{K}_H X_{tot}(k=0)\right)^{-1} \\ X_{ext}(k) &\xrightarrow{k\to 0} \bar{X}_{ext}\left(1 - \frac{4\pi}{\Omega} P^\dagger \hat{k}\hat{k}^\dagger P \bar{X}_{ext}\right)^{-1}, \end{aligned} \tag{5.26}$$

as may be verified by direct substitution, where $\bar{X}_{ext}$ represents what would be obtained for $\bar{X}_{tot}(k)$ if only the regular parts of $\bar{K}(k)$ were relevant.

Finally, substituting (5.26) into (5.24) yields an expression whose inverse gives $\left(\epsilon^{-1}_{0,0}(k)\right)^{-1} = 1 - \frac{4\pi}{\Omega}\hat{k}^\dagger P \bar{X}_{ext} P^\dagger \hat{k} + O(k)$, as may be verified directly by multiplication

to yield the identity. Substituting this last result in (5.20) and using the fact that $\hat{k}^\dagger \hat{k} = 1$ shows that the $k \to 0$ limit has precisely the correct tensor character, and gives the final result for the macroscopic dielectric tensor,

$$\bar{\epsilon} = 1 - \frac{4\pi}{\Omega} P \bar{X}_{ext} P^\dagger, \tag{5.27}$$

with $\bar{X}_{ext}$ defined explicitly as the $k \to 0$ limit in (5.26).

5.5 Computational Details

The density-functional theory calculations and the subsequent dielectric calculations were performed in the open source code JDFTx [82], following the procedure outlined in 5.1. All calculations utilized GGA pseudopotentials generated in Opium.

The ice is a two-molecule face centered cubic structure, from [64], with the unit cell size optimized, yielding a lattice constant of 5.88 bohr, with the single molecule of water for the additive approximation calculation in a box three times this lattice constant. The water and ice calculations utilize a plane-wave cutoff of 30 H (hartree), a sufficiently large cutoff as determined from convergence studies with the oxygen pseudopotential. The molecular water band structure calculations use 1000 bands, with the additive approximation calculations using those 1000 bands to produce 500 eigenvectors. The number of necessary eigenvectors is actually much smaller than this, as demonstrated in Figure 5.2, which shows the rapid convergence of the bulk dielectric constant of ice with the number of included eigenvectors. The crystalline ice calculation utilized 500 bands.

The carbon positions in the crystalline, four molecule unit cell, benzene geometry are from [15], and the hydrogen positions are from an isolated benzene molecule calcu-

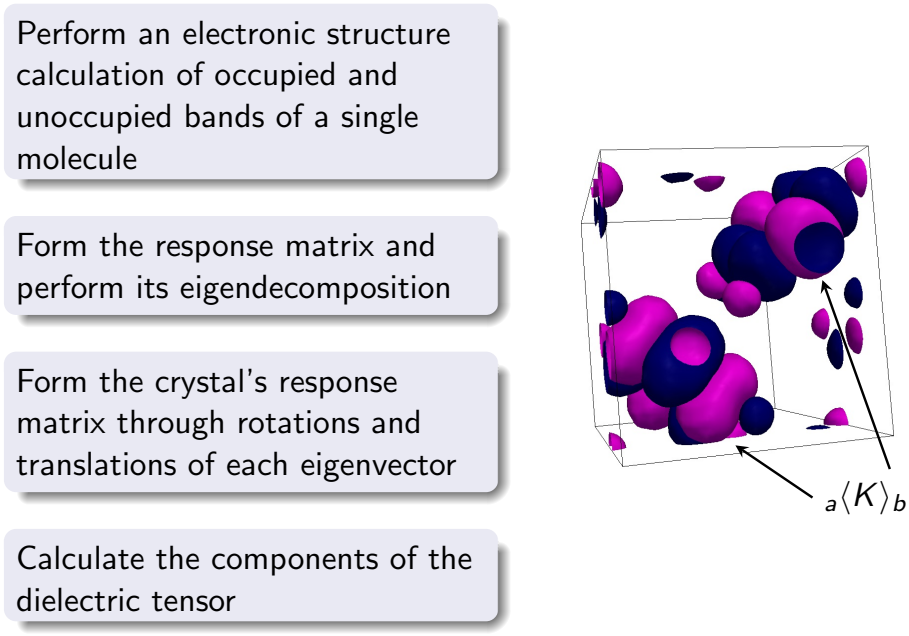

Figure 5.1: Calculations utilizing the additive approximations, such as the dielectric tensor calculation, can be broken into the above steps.

lation, with the single benzene molecule for the additive approximation calculation in a box the same size as the crystalline unit cell. The additive approximation calculations for benzene utilize a plane-wave expansion with a cutoff of 25 H, and these calculations utilize 600 bands per molecule, with the additive approximation using 600 eigenvectors per molecule. The carbon pseudopotential is softer than the oxygen pseudopotential used in the water calculation, so a smaller cutoff can be used. The benzene crystal calculation used 600 bands, with a cutoff of 20 H. The lower plane-wave cutoff for the benzene crystal calculation was necessary because of the large memory requirements of the calculation.

5.6 Results

The bulk dielectric constant can be evaluated for the crystal in either the full calculation or the additive approximations of the form (5.8) for either χ_{ni} or χ_{tot}. The dielectric constant must be converged with regards to plane-wave cutoff, number of included bands, and, for the additive approximations, the number of included eigenvectors. For the additive approximations, the number of included bands and eigenvectors is *per molecule*, whereas for the crystalline case, the number of included bands is *per unit cell*, so that the number of included bands for the molecular case should be N times faster than for the crystal, where N is the number of molecules per unit cell. Figure 5.2 shows the convergence of the benzene and ice crystals within the additive approximation of the form (5.8) for χ_{tot}. The solid lines show convergence of the dielectric constant with number of eigenvectors, with the number of bands is constant, at 1000 for water, and 600 for benzene. While the dielectric constant converges at around 100 included eigenvectors for ice, more eigenvectors are necessary for the benzene crystal. The dotted lines in the figure depict the convergence of the dielectric constant as the number of bands and number of eigenvectors increase, such that the number of conduction-valence pairs is equal to the number of included eigenvectors. The dotted lines converge much slower than the solid lines, indicating that the eigenvector basis is a better basis than the conduction-valence pair basis. The ice calculation appears to be well-converged, while the benzene calculation may not be completely converged.

The dielectric bands for an ice crystal, and the dielectric levels for a single, isolated water molecule can be computed, as shown in Figure 5.3. The molecular and crystal levels are similar, but the molecule does not have the k-point dependent band structure of the crystal. The molecular dielectric levels are split by the exchange-correlation and Coulomb interactions between the molecules, as shown in the crystalline dielectric band

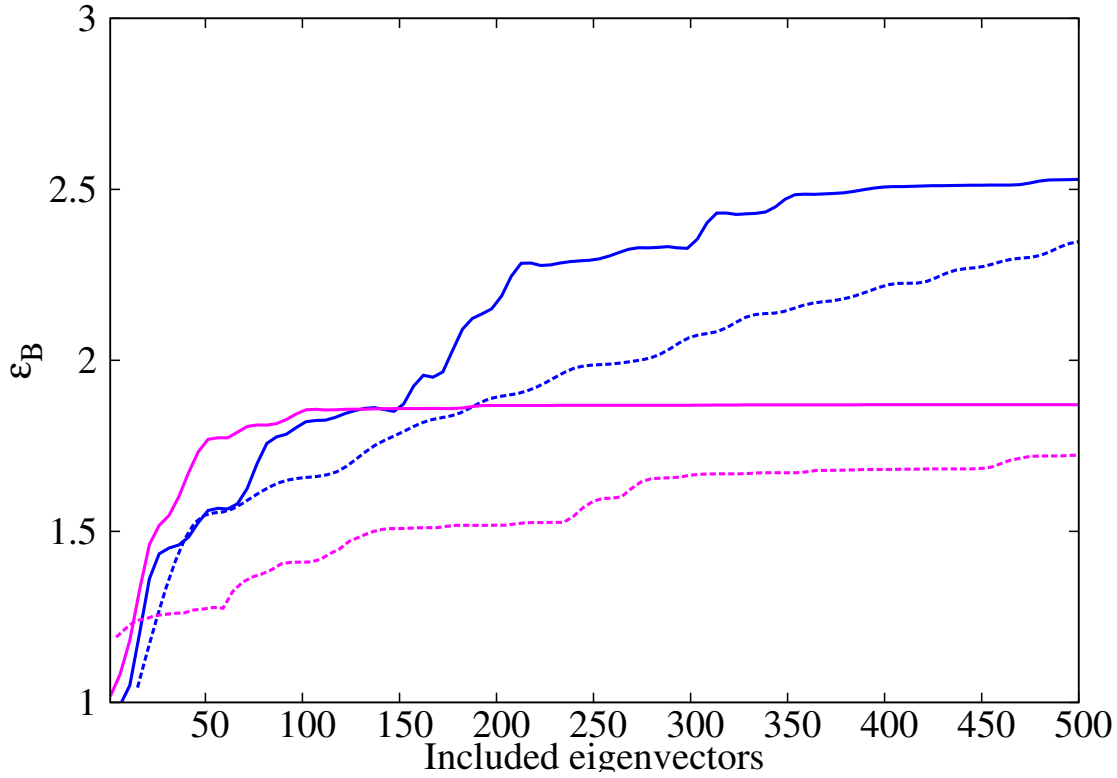

Figure 5.2: This figure demonstrates the convergence of the average bulk dielectric constant (from Eq. 5.27) for benzene (blue lines converging around 2.5) and ice (lower purple lines converging around 1.8) using the additive approximation for χ_{tot} in the form (5.8) with the number of included eigenvectors per molecule at constant number of bands (solid lines) and with number of included eigenvectors equal to the number of conduction-valence orbital pairs per molecule (dotted lines).

plot of Figure 5.3. For instance, the lowest molecular dielectric level in the figure splits into two levels in the crystalline calculation, which has two water molecules per unit cell.

The additive approximation can be utilized to produce dielectric band structures which very closely approximate that of the crystal, as shown in Figure 5.4. The dielectric band structure from the χ_{tot} additivity approximation of the form (5.8) most closely resembles that of the crystal, whereas the χ_{ni} additivity approximation results in slightly

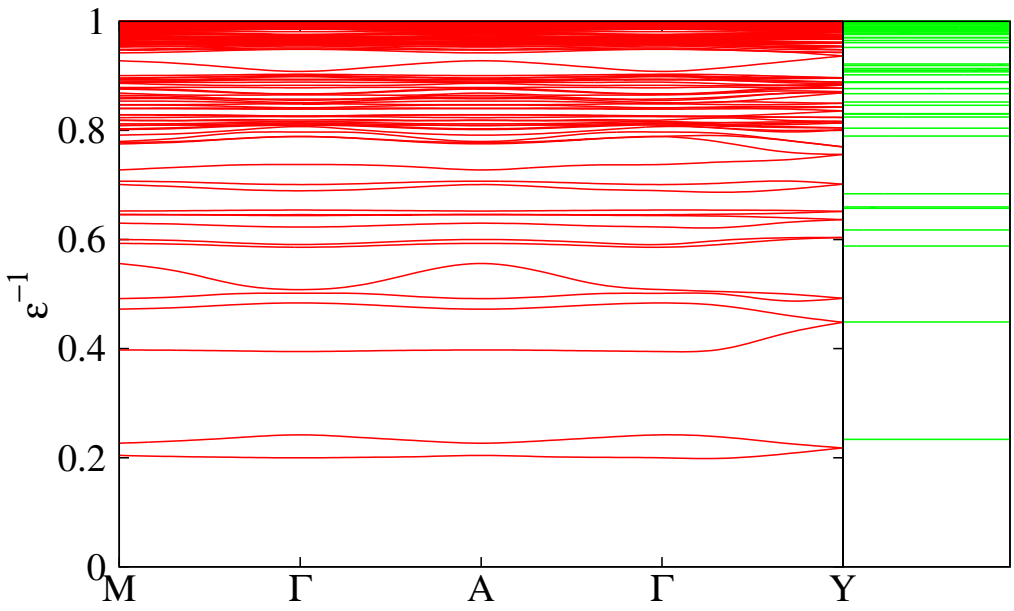

Figure 5.3: Dielectric band structure of ice, and the molecular band levels for water, both with GGA.

less band splitting, due to the underestimation of the interactions between molecules in the crystal. However, the χ_{tot} additivity approximation does slightly underestimate the dispersion of the full crystalline calculation. This potentially could be somewhat corrected in future work by including an additional intermolecular kinetic energy term, such as a Thomas-Fermi estimate of the kinetic energy correction.

The additive approximations can be applied using any density functional, or applied with quantum chemistry calculations. Shown in Figure 5.5, the results for ice are not strongly functional dependent, with LDA and GGA producing very few differences between the dielectric band structure plots.

The same procedure can be applied to other systems, such as crystalline benzene,

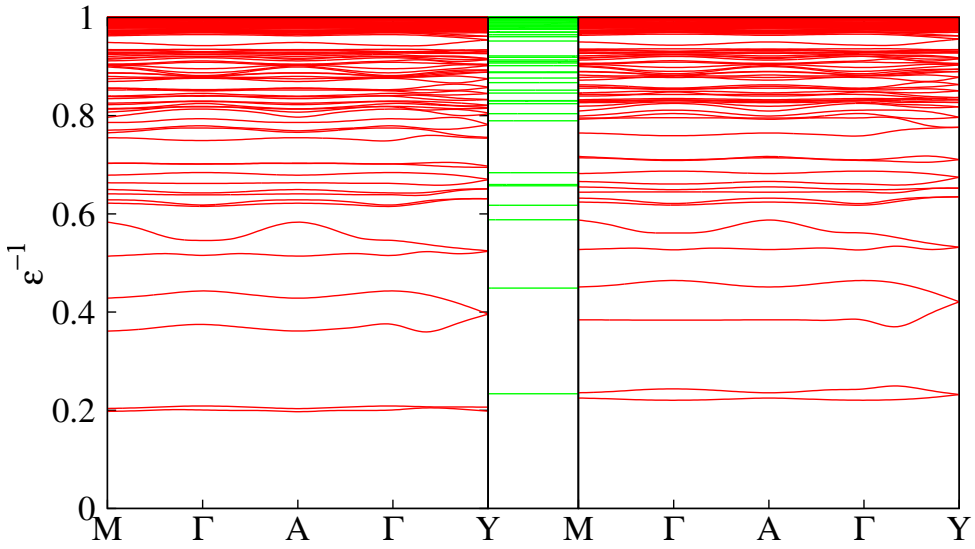

Figure 5.4: Ice dielectric band structure in the additive approximations of the form (5.8) for χ_{ni} and χ_{tot}, left and right images respectively, within GGA. Molecular levels are shown in green between the two band structures for reference.

although with four molecules per unit cell, the splittings are more complicated and difficult to distinguish. Figure 5.6 demonstrates the remarkably good agreement between benzene additive approximation calculations and crystalline ones.

5.7 Conclusion

This chapter develops in detail a theoretical approach to the determination of the full, microscopic dielectric response of molecular crystals. We argue that not only the non-interacting but also the total microscopic susceptibility linear response functional can be decomposed, to a good approximation, into a sum of individual molecular contributions. We further show that eigenvectors of the individual molecular response function form a

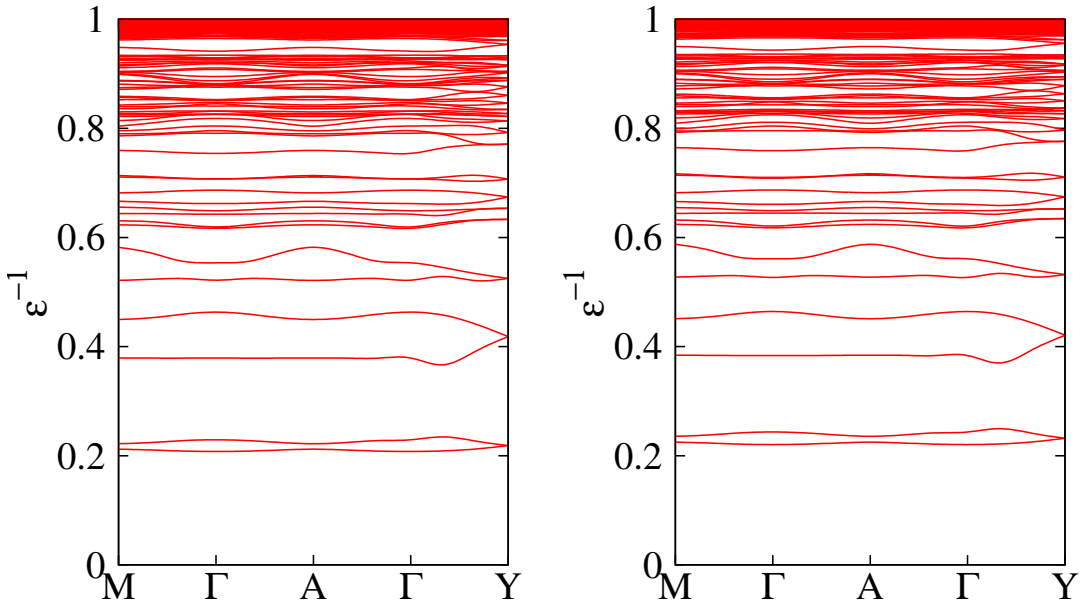

Figure 5.5: Ice dielectric band structure in the additive approximation, with sum of total dielectric matrices, LDA and GGA.

good basis for the description of the response of the overall system.

We then demonstrated the feasibility of the approach by using it to compute detailed dielectric band structures, and validated the approach by finding excellent agreement with far more expensive direct, full crystal calculations. We also presented a clear formalism for computing the macroscopic dielectric tensor of a molecular crystal without having to resort to the approximations inherent in the Clausius-Mossotti relation, which treats each molecule (or atomic group) as a polarizable dipole, and, in its most basic form, does not address the directionality of the polarizability.

The next steps in this work would be to explore the procedures we developed for employing quantum chemical methods which include higher-order correlation effects.

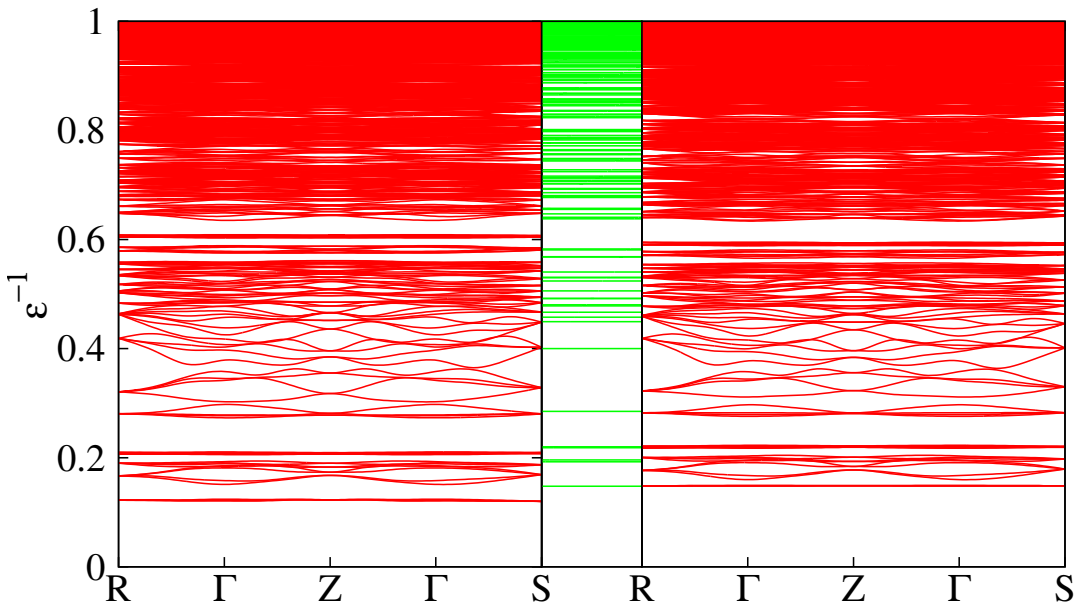

Figure 5.6: From left to right, the benzene crystal, molecule, and total dielectric additive approximation calculations, all with GGA

This would require a series of response calculations for a single molecule, allowing us to build a *nearly fully correlated* dielectric response function for the *entire* crystal. It would then be promising to explore the dielectric response of molecular crystals where the molecular polarizabilities are strongly affected by correlation effects. A final direction of interest would be to develop methods which generalize this approach to molecular fluids, where statistical averaging over differing arrangements of molecules would be required.

CHAPTER 6

OUTLOOK

This thesis has explored the practice of and approximations involved in partitioning systems into a molecule or surface treated at one level of theory, and a surrounding fluid or other molecular environment treated with another theory. Through a combination of both theory and application, the *ab initio* calculations in this thesis elucidated properties of molecules and solids. While the contents of each chapter represent discrete projects, promising future projects combine the findings and techniques of other chapters, creating new possibilities.

Chapter 2 describes a method for solvating molecules, clusters, and surfaces with an external potential, for instance, from joint density-functional theory solvation. Chapter 3 investigates equilibrium and kinetic behavior of the lithium sulfur battery system. The continuation of these projects naturally could involve calculations of sulfur anions with joint density functional theory ionic solvation, including geometry optimization, followed by quantum Monte Carlo calculations, especially of the monoanions that may benefit from a many-body treatment. The increased accuracy of both quantum Monte Carlo and joint density functional theory, combined with the inclusion of ionic solvation could bring the theoretical results of Chapter 3 into even closer agreement with experiment.

In Chapter 4, defects in pentacene thin films are examined using a polarizable continuum solvation model and time-dependent density-functional theory. The last chapter investigates the dielectric matrix, and approximations of the dielectric matrix of an entire system (a crystal or a snapshot of a fluid) from calculations performed on a single molecule. A next step would be to evaluate the effectiveness of using a polarizable continuum solvation model in Chapter 4 by re-visiting the calculations using the techniques

developed in Chapter 5. To do this, one would begin by calculating the full, microscopic dielectric properties of the entire pentacene crystal through application of the molecular decomposition developed and validated in Chapter 5. With this dielectric response in hand, one would then perform time-dependent density-functional theory calculations to validate the results from Chapter 4, and could then go on to more reliable GW/Bethe-Salpeter Equation calculations of the optical properties of these pentacene defects.

In summary, I have found that approaches to molecular systems, either liquid or solid, which decompose the system into a solute (or single molecule in a crystal) treated at a higher level of theory and a solvent (or environment) treated at another level of theory are not only computationally viable but also can lead to reliable predictions of importance to realistic systems. These approaches, moreover, can be applied to a variety of physical properties, from solution concentrations under varying electrochemical conditions to dielectric properties, and to a wide range of levels of theory, from chemically-accurate diffusion Monte Carlo to density-functional theory and time-dependent density-functional theory. Having succeeded with such a broad range of systems, properties, and theoretical techniques, I recommend that such approaches continue to be developed to reach even higher degrees of realism, accuracy, and cost-effectiveness. Ultimately, with enough examples in hand, it would be good to consider whether a formal theoretical framework, or at least a set of guiding principles, could be developed to encompass all such approaches generally.

APPENDIX A

GAUSSIAN INPUT FOR PENTACENE DEFECTS

Below is an example input file for a TDDFT calculation for a defect molecule in a pentacene crystal. These calculations took on the order of one day, using the Gaussian program licensed through theCornell Chemistry Department.

The geometry must first be optimized, and then a TDDFT calculation, using the same functional and basis set, can be performed.

The first line of the input file gives the functional and basis set, followed by the TDDFT command which identifies the number of excited states to be calculated. The next command gives information about the solvation, particularly that the Gaussian program should expect to read information about the solvent after the geometry of the molecule. The next line is blank, followed by the title line, followed by a blank line, and then the charge and spin multiplicity of the molecule. Next, the coordinates in angstroms of each of the atoms in the molecule are listed, followed by a blank line and the solvent information. In this case, the dielectric constant of the solvent is given as 4.82. After the solvent line, a blank line is required by the Gaussian program.

The original guess for the molecular coordinates can be obtained from crystalline data, or from a geometry optimization using a molecular mechanics program such as avogadro. If the molecular mechanics program is used, an initial guess structure is drawn, then the molecular mechanics force fields are used to create a better guess. Subsequently, a geometry optimization in the Gaussian program is run, using a small basis set. The basis set size is then increased. Geometries are typically fairly accurate with small basis sets, so considerable computer time can be saved with this strategy.

B3LYP/6-311++G(d,p) TD=(NStates=6) SCRF=(Solvent=Generic,Read)

pentacene

0 1

C -1.207841 0.697363 0.000000

...etc. for each atom in the molecule

H -0.000040 -2.479099 0.000000

solventname=pentacene

eps=4.82

APPENDIX B

SULFUR ANION GEOMETRIES

Below are the optimized geometries from the lithium sulfur species used in Figure 3.2. Each species is included with information necessary to create the Gaussian input file used to produce the *ab initio* calculations for Figure 3.2. Each geometry listed is a stationary point for a calculation with no ionic effects included.

Input file:

#B3LYP/6-311++G(2df) SCF=Tight SCRF=(PCM,Read,Solvent=TetraHydroFuran)

title card

N M X
Eps=37

where N is the charge, M is the spin multiplicity, and X is the geometry, as shown in the table, from left to right, as Species label, N M X (in Angstroms):

S_1^{1-}	-1	2	-9.094675	6.661986	0.000000
S_1^{2-}	-2	1	1.754423	-0.396222	0.000000
S_2^{1-}	-1	2	-9.060266	6.661986	0.000000
			-7.034409	6.661980	0.000000
S_2^{2-}	-2	1	-9.140856	6.661986	0.000000
			-6.953819	6.661980	0.000000
S_3^{1-}	-1	2	1.692730	-0.364708	0.000000
			-0.000002	0.729426	0.000000
			-1.692728	-0.364718	0.000000
S_3^{2-}	-2	1	1.742370	-0.402987	0.000000
			-0.000002	0.805986	0.000000
			-1.742369	-0.402998	0.000000
S_4^{1-}	-1	2	-0.136449	-0.325006	1.742712
			-0.448737	1.011088	-1.511764
			0.204219	-0.862061	-1.615011
			0.398192	-1.690178	0.402549
S_4^{2-}	-2	1	0.256757	-0.561154	2.085853
			-0.719160	0.905647	-2.006456
			0.604442	-0.596290	-1.369650
			-0.124814	-1.614359	0.308740
S_5^{1-}	-1	2	1.613768	-0.625288	-0.423519
			-0.000518	-1.313162	0.748643
			-1.614217	-0.624123	-0.423459
			-2.044380	1.282055	0.049161
			2.045348	1.280518	0.049174
S_5^{2-}	-2	1	1.610040	-0.629130	-0.416861
			-0.000468	-1.322304	0.757104
			-1.610559	-0.628272	-0.416607
			-2.005413	1.290525	0.038074
			2.006402	1.289183	0.038289
S_6^{1-}	-1	2	-4.076000	2.304024	0.169046
			-2.552218	1.073693	0.601522
			-1.087112	1.106707	-0.850827
			0.121090	2.909459	-0.639583
			1.621190	2.587171	0.739835
			3.130130	1.506237	-0.019993
S_6^{2-}	-2	1	-4.089318	2.313683	0.257150
			-2.482465	1.051914	0.608383
			-1.095126	1.149543	-0.942799
			0.126749	2.890910	-0.739110
			1.551668	2.606081	0.753835
			3.145571	1.475159	0.062541

S_7^{1-}	-1	2	-2.068581	2.370279	0.686511
			-0.275054	2.440397	-0.374855
			1.022540	0.969426	0.331479
			0.560286	-0.810130	-0.725816
			-0.498214	-2.038952	0.476587
			-3.305870	-0.767073	0.795513
			-3.294683	0.939098	-0.285211
S_7^{2-}	-2	1	-2.059131	2.297411	0.861999
			-0.459670	2.196363	-0.542538
			1.106539	0.972536	0.154293
			1.072295	-0.949284	-0.673516
			0.237183	-2.331647	0.618500
			-3.972630	-0.549347	0.440029
			-3.784162	1.467013	0.045442
S_8	0	1	-2.120731	2.398085	0.738822
			-0.338257	2.319614	-0.331072
			0.842361	0.798682	0.456700
			0.611526	-0.899469	-0.722727
			-0.777654	-2.154196	0.184763
			-2.629204	-1.856276	-0.715824
			-3.740756	-0.554765	0.466629
			-3.578977	1.362775	-0.323889
S_8^{1-}	-1	2	-2.124249	2.691080	0.695534
			-0.283851	2.586854	-0.229293
			0.748148	0.906529	0.484391
			0.505961	-0.994298	-0.739848
			-0.779396	-2.430482	0.078013
			-2.678496	-2.139761	-0.671743
			-3.645686	-0.665331	0.463361
			-3.474122	1.459860	-0.327013
S_8^{2-}	-2	1	-5.439950	-0.410056	1.280766
			2.911770	-0.272966	-1.642910
			2.488847	0.501361	0.224377
			0.898860	-0.496878	1.124069
			-0.922381	0.392468	0.513045
			-1.688291	-0.697530	-1.092975
			-2.992477	-2.184228	-0.337971
			-4.951827	-1.484821	-0.413881

S_9^{2-}	-2	1	-1.833512	1.930693	1.262848
			-0.447367	2.226300	-0.297140
			1.052713	0.796501	-0.179309
			0.618933	-0.883229	-1.397281
			-0.104062	-2.439986	-0.217473
			1.451486	-3.457486	0.683177
			-4.000966	-1.200742	-1.530358
			-4.264958	-0.438283	0.367485
			-3.753957	1.580681	0.461449
S_{10}^{1-}	-1	2	-2.269345	2.208597	1.155892
			0.239377	1.777718	-0.390692
			1.534292	0.210277	-0.133458
			1.206855	-1.256784	-1.603969
			-0.160162	-2.700225	-0.856315
			0.898030	-4.355911	-0.166569
			1.489324	-4.126486	1.803262
			-4.606526	-1.126088	-0.797086
			-5.104111	0.349503	0.583336
			-4.059424	2.133846	0.159001

BIBLIOGRAPHY

[1] C. Amovilli, C. Filippi, and F. M. Floris. Coupling quantum Monte Carlo to a nonlinear polarizable continuum model for spherical solutes. *J. Phys. Chem. B.*, 110(51):26225–26231, Jan 2006.

[2] C. Amovilli, C. Filippi, and F. M. Floris. Quantum Monte Carlo formulation of volume polarization in dielectric continuum theory. *J. Chem. Phys.*, 129(24):244106, Jan 2008.

[3] J. E. Anthony. Functionalized acenes and heteroacenes for organic electronics. *Chem. Rev.*, 106:5028, 2006.

[4] S. Arrhenius. Development of the theory of electrolytic dissociation. *Proceedings of the Royal Institution*, 1904.

[5] R. Assaraf, M. Caffarel, and A. Scemama. Improved Monte Carlo estimators for the one-body density. *Phys. Rev. E*, 75(3):1–4, Mar 2007.

[6] C. Barchasz, F. Molton, C. Duboc, J. Lepretre, S. Patoux, , and F. Alloin. Lithium/sulfur cell discharge mechanism: An original approach for intermediate species identification. *Anal. Chem.*, 84:39733980, 2012.

[7] V. Barone, M. Cossi, and J. Tomasi. A new definition of cavities for the computation of solvation free energies by the polarizable continuum model. *J. Chem. Phys.*, 107(8):3210–3221, Jan 1997.

[8] R. Bauernschmitt and R. Ahlrichs. Treatment of electronic excitations within the adiabatic approximation of time dependent density functional theory. *Chem. Phys. Lett.*, 256:454, 1996.

[9] A. D. Becke. Density-functional thermochemistry. iii. the role of exact exchange. *J. Chem. Phys.*, 98:5648, 1993.

[10] T. C. Berkelbach, M. S. Hybertsen, and D. R. Reichman. Microscopic theory of singlet exciton fission. i. general formulation. *J. Chem. Phys.*, 138:114102, 2013.

[11] M. Breban, D. B. Romero, S. Mezhenny, V. W. Ballarotto, and E. D. Williams. Photocurrent probe of field-dependent mobility in organic thin-film transistors. *Appl. Phys. Lett*, 87:203503, 2005.

[12] F. Bruneval and X. Gonze. Accurate GW self-energies in a plane-wave basis using only a few empty states: Towards large systems. *Phys. Rev. B*, 78:085125, 2008.

[13] M. Burkatzki, C. Filippi, and M. Dolg. Energy-consistent pseudopotentials for quantum Monte Carlo calculations. *J. Chem. Phys.*, 126, Jan 2007.

[14] H. Min Cho and W. A. Lester. Explicit solvent model for quantum Monte Carlo. *J. Phys. Chem. Lett.*, 1(23):3376–3379, Dec 2010.

[15] E.G. Cox, D.W.J. Cruickshank, and J.A.S. Smith. The crystal structure of benzene at -3° C. *Proc. R. Soc. Lond. A*, 247, 1958.

[16] N. D. Drummond, M. D. Towler, and R. J. Needs. Jastrow correlation factor for atoms, molecules, and solids. *Phys. Rev. B*, 70:235119, 2004.

[17] J. Fattebert and F. Gygi. First-principles molecular dynamics simulations in a continuum solvent. *Int J Quantum Chem*, 93(2):139–147, Jan 2003.

[18] A.M. Fernandez-Escamilla, M.S. Cheung, M.C. Vega, M. Wilmanns, J.N. Onuchic, and L. Serrano. Solvation in protein folding analysis: Combination of theoretical and experimental approaches. *P Natl Acad Sci USA*, 101(9):2834–2839, Jan 2004.

[19] S. Forrest. The path to ubiquitous and low-cost organic electronic appliances on plastic. *Nature*, 428:911–918, 2004.

[20] W.M.C. Foulkes, L. Mitas, R.J. Needs, and G. Rajagopal. Quantum Monte Carlo simulations of solids. *Rev. Mod. Phys.*, 73(1):33–83, Jan 2001.

[21] M. J. Frisch, G. W. Trucks, H. B. Schlegel, G. E. Scuseria, M. A. Robb, J. R. Cheeseman, G. Scalmani, V. Barone, B. Mennucci, G. A. Petersson, H. Nakatsuji, M. Caricato, X. Li, H. P. Hratchian, A. F. Izmaylov, J. Bloino, G. Zheng, J. L. Sonnenberg, M. Hada, M. Ehara, K. Toyota, R. Fukuda, J. Hasegawa, M. Ishida, T. Nakajima, Y. Honda, O. Kitao, H. Nakai, T. Vreven, J. A. Montgomery Jr., J. E. Peralta, F. Ogliaro, M. Bearpark, J. J. Heyd, E. Brothers, K. N. Kudin, V. N. Staroverov, R. Kobayashi, J. Normand, K. Raghavachari, A. Rendell, J. C. Burant, S. S. Iyengar, J. Tomasi, M. Cossi, N. Rega, J. M. Millam, M. Klene, J. E. Knox, J. B. Cross, V. Bakken, C. Adamo, J. Jaramillo, R. Gomperts, R. E. Stratmann, O. Yazyev, A. J. Austin, R. Cammi, C. Pomelli, J. W. Ochterski, R. L. Martin, K. Morokuma, V. G. Zakrzewski, G. A. Voth, P. Salvador, J. J. Dannenberg, S. Dapprich, A. D. Daniels, . Farkas, J. B. Foresman, J. V. Ortiz, J. Cioslowski, and D. J. Fox. Gaussian 09, revision a.1;. Gaussian Inc., Wallingford, CT, 2009.

[22] F. Gaillard and E. Levillain. Visible time-resolved spectroelectrochemistry: application to study of the reduction of sulfur(S8) in dimethylformamide. *Journal of Electroanalytical Chemistry*, 398, 1995.

[23] S. Grimme and M. Parac. Substantial errors from time-dependent density functional theory for the calculation of excited states of large systems. *Chem. Phys. Chem.*, 4:292, 2003.

[24] J. Grossman and L. Mitas. Efficient quantum Monte Carlo energies for molecular dynamics simulations. *Phys. Rev. Lett.*, 94(5):1–4, Feb 2005.

[25] G. Gu and M. G. Kane. Moisture induced electron traps and hysteresis in pentacene-based organic thin-film transistors. *Appl. Phys. Lett.*, 92:053305, 2008.

[26] E. B. Guidez and C. M. Aikens. Origin and TDDFT benchmarking of the plasmon resonance in acenes. *J. Phys. Chem. C*, 117:21466–21475, 2013.

[27] M. Hagan, P. Schiffels, M. Hammer, S. Dorfler, J. Tubke, M. Hoffmann, H. Althues, and S. Kaskel. In-situ raman investigation of polysulfide formation in Li-S cells. *Journal of the Electrochemical Society*, 160, 2013.

[28] D. Han, B. Kim, S. Choi, Y. Jung, J. Kwak, , and S. Park. Time-resolved in situ spectroelectrochemical study on reduction of sulfur in n,n'-dimethylformamide. *Journal of The Electrochemical Society*, 151:E283–E290, 2004.

[29] H. Heitzer, T. Marks, and M. Ratner. First-principles calculation of dielectric response in molecule-based materials. *JACS*, 136:9753–9759, 2013.

[30] M.S. Hybertsen and S.G. Louie. *Ab initio* static dielectric matrices from the density-functional approach. i. formulation and application to semiconductors and insulators. *Physical Review B*, 35:5585–5601, 1987.

[31] M. J. Jaquith, J. E. Anthony, and J. A. Marohn. Long-lived charge traps in functionalized pentacene and anthradithiophene studied by time-resolved electric force microscopy. *J. Mater. Chem.*, 19:6116, 2009.

[32] C. Jeffery and P. Austin. A new analytic equation of state for liquid water. *J. Chem. Phys.*, 110:484, 1999.

[33] C. Jundt, G. Klein, B. Sipp, J. Lemoigne, M. Joucla, and A. A. Villaeys. Exciton dynamics in pentacene thin films studied by pump-probe spectroscopy. *Chem. Phys. Lett.*, 241:84, 1995.

[34] Y. Jung, S. Kim, B. Kim, D. Han, S. Park, and J. Kwak. Effect of organic solvents and electrode materials on electrochemical reduction of sulfur. *Int. J. Electrochem. Sci.*, 3, 2008.

[35] E. S. Kadantsev, M. J. Stott, and A. Rubio. Electronic structure and excitations in oligoacenes from *ab initio* calculations. *J. Chem. Phys.*, 124:134901, 2006.

[36] J. H. Kang, D. da Silva, J. L. Bredas, and X. Y. Zhu. Shallow trap states in pentacene thin films from molecular sliding. *Appl. Phys. Lett.*, 86:152115, 2005.

[37] B. Kim and S. Park. In situ spectroelectrochemical studies on the reduction of sulfur in dimethyl sulfoxide solutions. *Journal of the Electrochemical Society*, 140, 1993.

[38] Y. Kim, C. J. Cramer, and D. G. Truhlar. Steric effects and solvent effects on s_N2 reactions. *Journal of Physical Chemistry A*, 113(32):9109–9114, Jan 2009.

[39] D. Knipp and J. E. Northrup. Electric-field-induced gap states in pentacene. *Adv. Mater.*, 21:2511, 2009.

[40] S. J. Konezny, M. N. Bussac, and L. Zuppiroli. Hopping and trapping mechanisms in organic field-effect transistors. *Phys. Rev. B*, 81:045313, 2010.

[41] D. V. Lang, X. Chi, T. Siegrist, A. M. Sergent, and A. P. Ramirez. Bias-dependent generation and quenching of defects in pentacene. *Phys. Rev. Lett.*, 93:076601, 2004.

[42] T. Lazaridis. "new view" of protein folding reconciled with the old through multiple unfolding simulations. *Science*, 278(5345):1928–1931, Dec 1997.

[43] E. Levillain, F. Gaillard, , and J.P. Lelieur. Polysulfides in dimethylformamide: only the redox couples S_n/S_{2n} are involved. *J. Electroanal. Chem.*, 440, 1997.

[44] E. Levillain, F. Gaillard, P. Leghie, A. Demortier, and J.P. Lelieur. On the understanding of the reduction of sulfur (S8) in dimethylformamide (dmf). *Journal of Electroanalytical Chemistry*, 420:167177, 1997.

[45] Y. Y. Lin, D. J. Gundlach, S. F. Nelson, and T. N. Jackson. Pentacene-based organic thin-film transistors. *IEEE Trans. Electron Device*, 44:1325, 1997.

[46] J. Lischner and T. A. Arias. Classical density-functional theory of inhomogeneous

water including explicit molecular structure and nonlinear dielectric response. *J. Phys. Chem. B*, 114(5):1946–1953, Jan 2010.

[47] D. Lu, F. Gygi, and G. Galli. Dielectric properties of ice and liquid water from first-principles calculations. *Physical Review Letters*, 100:147601, 2008.

[48] J. L. Luria, K. A. Schwarz, M. J. Jaquith, R. G. Hennig, and J. A. Marohn. Spectroscopic characterization of charged defects in polycrystalline pentacene by time- and wavelength-resolved electric force microscopy. *Advanced Materials*, 23:624, 2010.

[49] M. Chiesa M. Tello, C. M. Duffy, and H. Sirringhaus. Charge trapping in intergrain regions of pentacene thin film transistors. *Adv. Funct. Mater.*, 18:3907, 2008.

[50] A. Maliakal, K. Raghavachari, H. Katz, E. Chandross, and T. Siegrist. Photochemical stability of pentacene and a substituted pentacene in solution and in thin films. *Chem. Mater.*, 16:4980, 2004.

[51] S. G. J. Mathijssen, M. Clle, H. Gomes, E. C. P. Smits, B. de Boer, I. McCulloch, P. A. Bobbert, and D. M. de Leeuw. Dynamics of threshold voltage shifts in organic and amorphous silicon field-effect transistors. *Adv. Mater.*, 19:2785, 2007.

[52] I. McCulloch, M. Heeney, C. Bailey, K. Genevicius, I. MacDonald, M. Shkunov, D. Sparrowe, S. Tierney, R. Wagner, W. Zhang, M. L. Chabinyc, R. J. Kline, M. D. McGehee, and M. F. Toney. Liquid-crystalline semiconducting polymers with high charge-carrier mobility. *Nature Materials*, 5:328 – 333, 2006.

[53] S. Miertus, E. Scrocco, and J. Tomasi. Electrostatic interaction of a solute with a continuum. a direct utilizaion of *ab initio* molecular potentials for the prevision of solvent effects. *Chem. Phys.*, 55:117, 1981.

[54] P. K. Nayak and N. Periasamy. Calculation of electron affinity, ionization potential, transport gap, optical band gap and exciton binding energy of organic solids using solvation model and DFT. *Org. Electron.*, 10:1396, 2009.

[55] R. Needs, M. Towler, N. Drummond, and P. Rios. Casino manual. *CASINO*, page 210, Jul 2008.

[56] NIST Computational Chemistry Comparison and Benchmark Database, NIST Standard Reference Database Number 101 Release 15b August 2011, Ed. Russell D. Johnson III, http://cccbdb.nist.gov .

[57] J. E. Northrup and M. L. Chabinyc. Gap states in organic semiconductors:hydrogen- and oxygen-induced states in pentacene. *Phys. Rev. B*, 68:041202, 2003.

[58] H. Ohtaki. Ionic solvation in aqueous and nonaqueous solutions. *Monatshefte für Chemie*, 132:1237–1268, 2001.

[59] C. Pannemann, T. Diekmann, and U. Hilleringmann. Degradation of organic field-effect transistors made of pentacene. *J. Mater. Res.*, 19:1999, 2004.

[60] R. Parr and W. Yang. *Density-Functional Theory of Atoms and Molecules*. Oxford University Press, New York, NY, 1989.

[61] S. A. Petrosyan, Jean-Francois Briere, David Roundy, and T. A. Arias. Joint density-functional theory for electronic structure of solvated systems. *Phys. Rev. B*, 75:205105, May 2007.

[62] S.A. Petrosyan, A.A. Rigos, and T.A. Arias. Joint density-functional theory: *Ab initio* study of Cr_2O_3 surface chemistry in solution. *J. Phys. Chem. B*, 109(32):15436–15444, Jan 2005.

[63] Y. Qiu, Y. C. Hu, G. F. Dong, L. D. Wang, J. F. Xie, and Y. N. Ma. H_2O effect on the stability of organic thin-film field-effect transistors. *Appl. Phys. Lett.*, 83:1644, 2003.

[64] Z. Raza, D. Alfé, C. G. Salzmann, J. Klimes, A. Michaelides, and B. Slater. Proton ordering in cubic ice and hexagonal ice; a potential new ice phase-XIc. *Phys. Chem. Chem. Phys.*, 13:19788–197595, 2011.

[65] C. K. Regan. Steric effects and solvent effects in ionic reactions. *Science*, 295(5563):2245–2247, Mar 2002.

[66] L. Reining, G. Onida, and R.W. Godby. Elimination of unoccupied state summations in *ab initio* self-energy calculations for large supercells. *Phys. Rev. B*, 56, 1997.

[67] Y.M. Rhee, E.J. Sorin, G. Jayachandran, E. Lindahl, and V.S. Pande. Simulations of the role of water in the protein-folding mechanism. *P Natl Acad Sci Usa*, 101(17):6456–6461, Jan 2004.

[68] V. Arkhipov S. Verlaak and P. Heremans. Modeling of transport in polycrystalline organic semiconductor films. *Appl. Phys. Lett.*, 82:745, 2003.

[69] A. Salleo, F. Endicott, and R. A. Street. Reversible and irreversible trapping at room temperature in poly(thiophene) thin-film transistors. *Appl. Phys. Lett.*, 86:263505, 2005.

[70] A. Salleo and R. A. Street. Light-induced bias stress reversal in polyfluorene thin-film transistors. *J. Appl. Phys.*, 94:471, 2003.

[71] K. Schwarz, R. Sundararaman, K. Letchworth-Weaver, and R. Hennig. Framework for solvation in quantum Monte Carlo. *Phys. Rev. B*, 85:201102(R), 2012.

[72] L. Sebastian and G. Weiser. Charge transfer transitions in solid tetracene and pentacene studied by electroabsorption. *Chem. Phys.*, 61:125, 1981.

[73] S.Guo, S. Kim, S. Mohapatra, Y. Qi, T. Sajoto, A. Kahn, S. R. Marder, and S. Barlow. n-doping of organic electronic materials using air-stable organometallics. *Advanced Materials*, 24:699–703, 2012.

[74] L. Shulenburger and T. Mattsson. Quantum Monte Carlo applied to solids. *Phys. Rev. B*, 88, 2013.

[75] L. M. Smieska, V. A. Pozdin, J. L. Luria, R. G. Hennig, M. A. Hines, C. A. Lewis, and J. A. Marohn. Following chemical charge trapping in pentacene thin films by selective impurity doping and wavelength-resolved electric force microscopy. *Adv. Func. Matt.*, 22:5096, 2012.

[76] M. B. Smith and J. Michl. Recent advances in singlet fission. *Annual Review of Physical Chemistry*, 64:361–386, 2013.

[77] R. Steudel. Inorganic polysulfides S_n^{2-} and radical anions $S_n^{\cdot-}$.

[78] R. Street, A. Salleo, and M. Chabinyc. Bipolaron mechanism for bias-stress effects in polymer transistors. *Phys. Rev. B*, 68:85316, 2003.

[79] R. A. Street. Thin-film transistors. *Adv. Mater.*, 21:2007, 2009.

[80] R. Sundararaman and TA Arias. Efficient classical density-functional theories of rigid-molecular fluids and a simplified free energy functional for liquid water. *Computer Physics Communications*, 2013.

[81] R. Sundararaman, K. Letchworth Weaver, and T. Arias. A computationally efficacious free-energy functional for studies of inhomogeneous liquid water. *ArXiv e-prints*, December 2011.

[82] R. Sundararaman, K. Letchworth-Weaver, and T. A. Arias. jdftx. *http://jdftx.sourceforge.net*, 2012.

[83] R. Sundararaman, K Letchworth-Weaver, and TA Arias. A computationally efficacious free-energy functional for studies of inhomogeneous liquid water. *J. Chem. Phys.*, 137:044107, 2012.

[84] M. L. Tiago, J. E. Northrup, and S. G. Louie. *Ab initio* calculation of the electronic and optical properties of solid pentacene. *Phys. Rev. B*, 67:115212, 2003.

[85] J Tomasi, B Mennucci, and R Cammi. Quantum mechanical continuum solvation models, Jan 2005.

[86] P. Umari, G. Stenuit, and S. Baroni. GW quasiparticle spectra from occupied states only. *Phys. Rev. B*, 81:115104, 2010.

[87] P. Umari, A. J. Willamson, G. Galli, and N. Marzari. Dielectric response of periodic systems from quantum Monte Carlo calculations. *Phys. Rev. Lett.*, 95:207602, 2005.

[88] C. Umrigar and C. Filippi. Energy and variance optimization of many-body wave functions. *Phys. Rev. Lett*, 94:150201, 2005.

[89] J. Veres, S. Ogier, G. Lloyd, and D. De Leeuw. Gate insulators in organic field-effect transistors. *Chem. Mater.*, 16:4543, 2004.

[90] A. Vollmer, O. Jurchescu, I. Arfaoui, I. Salzmann, T. Palstra, P. Rudolf, J. Niemax, J. Pflaum, J. Rabe, and N. Koch. The effect of oxygen exposure on pentacene electronic structure. *Eur. Phys. J. E*, 17:339, 2005.

[91] H. Wilson, F. Gygi D. Lu, and G. Galli. Iterative calculations of dielectric eigenvalue spectra. *Physical Review B*, 79:245106, 2009.

[92] H. Wilson, F. Gygi, and G. Galli. Efficient iterative method for calculations of dielectric matrices. *Physical Review B*, 78:113303, 2008.

[93] H. Yang, L. Yang, M.-M. Ling, S. Lastella, D. D. Gandhi, G. Ramanath, Z. Bao, and C. V. Ryu. Aging susceptibility of terrace-like pentacene films. *J. Phys. Chem. C*, 112:16161, 2008.

[94] S. Yoo, B. Domercq, and B. Kippelen. Efficient thin-film organic solar cells based on pentacene/C_{60} heterojunctions. *Appl. Phys. Lett.*, 85:5427, 2004.

[95] Z. T. Zhu, J. T. Mason, R. Dieckmann, and G. G. Malliaras. Humidity sensors based on pentacene thin-film transistors. *Appl. Phys. Lett.*, 81:4643, 2002.

[96] P. M. Zimmerman, Z. Zhang, and C. B. Musgrave. Singlet fission in pentacene through multi-exciton quantum states. *Nature Chemistry*, 2:648652, 2010.